Cytoplasmic dynein regulates its attachment to microtubules via nucleotide state-switched mechanosensing at multiple AAA domains

Matthew P. Nicholas[a,b], Florian Berger[c,d,e], Lu Rao[a], Sibylle Brenner[a], Carol Cho[f], and Arne Gennerich[a,1]

[a]Department of Anatomy and Structural Biology, Gruss Lipper Biophotonics Center, and [b]Medical Scientist Training Program, Albert Einstein College of Medicine, Bronx, NY 10461; [c]Theory and Bio-Systems, Max Planck Institute of Colloids and Interfaces, 14424 Potsdam, Germany; [d]Laboratory of Sensory Neuroscience, and [e]Howard Hughes Medical Institute, Rockefeller University, New York, NY 10065; and [f]Department of Biochemistry, Stanford University School of Medicine, Stanford, CA 94305

Cytoplasmic dynein is a homodimeric microtubule (MT) motor protein responsible for most MT minus-end–directed motility. Dynein contains four AAA+ ATPases (AAA: ATPase associated with various cellular activities) per motor domain (AAA1–4). The main site of ATP hydrolysis, AAA1, is the only site considered by most dynein motility models. However, it remains unclear how ATPase activity and MT binding are coordinated within and between dynein's motor domains. Using optical tweezers, we characterize the MT-binding strength of recombinant dynein monomers as a function of mechanical tension and nucleotide state. Dynein responds anisotropically to tension, binding tighter to MTs when pulled toward the MT plus end. We provide evidence that this behavior results from an asymmetrical bond that acts as a slip bond under forward tension and a slip-ideal bond under backward tension. ATP weakens MT binding and reduces bond strength anisotropy, and unexpectedly, so does ADP. Using nucleotide binding and hydrolysis mutants, we show that, although ATP exerts its effects via binding AAA1, ADP effects are mediated by AAA3. Finally, we demonstrate "gating" of AAA1 function by AAA3. When tension is absent or applied via dynein's C terminus, ATP binding to AAA1 induces MT release only if AAA3 is in the posthydrolysis state. However, when tension is applied to the linker, ATP binding to AAA3 is sufficient to "open" the gate. These results elucidate the mechanisms of dynein–MT interactions, identify regulatory roles for AAA3, and help define the interplay between mechanical tension and nucleotide state in regulating dynein motility.

cytoplasmic dynein | mechanosensing | optical tweezers | AAA+ ATPases | microtubules

Numerous eukaryotic cellular processes require motion and force generated by cytoskeletal motor proteins, among which cytoplasmic dynein (hereinafter, "dynein") is unique for its size, complexity, and versatility. As a homodimeric, divergent AAA+ ATPase (AAA: ATPase associated with various cellular activities), dynein drives the majority of microtubule (MT) minus-end–directed motility in most eukaryotes (1). The motor functions as a massive protein complex (2), but its catalytic core consists of two identical heavy chains, each with six AAA modules (AAA1–6) linked in tandem to form a ring (Fig. 1A). AAA1–4 bind nucleotides, whereas AAA5 and -6 are structural (3, 4). A ∼15-nm "stalk" emerging from AAA4 (3, 4) separates the AAA modules from the MT-binding domain (MTBD). The stalk configuration influences both MT affinity and ATPase activity (5) and thereby mediates bidirectional allosteric communication between the AAA ring and the MTBD (3, 6). Finally, a ∼10-nm "linker" also emerges from the ring and undergoes cyclic reorientations that generate force and displacement (7–9).

For dynein to "walk," one motor domain ("head") must remain MT-bound while the other moves (10–13), thus requiring coordination of the "internal" cycles of both heads. Dynein may use allosteric mechanosensing (possibly through the stalk) to differentiate between the leading and trailing heads, because they experience oppositely directed mechanical tension (Fig. 1A). Kinesin (14–16) and myosin (17–19) use similar mechanisms, exhibiting asymmetry in filament binding and nucleotide affinity in response to applied forces.

Recent studies suggest dynein stepping is indeed tension regulated. The farther apart its heads are spread on the MT (i.e., the greater the intramolecular tension), the shorter the dwell time before the next step and the greater the probability of the rear head advancing (12, 13). We demonstrated ATP-independent, force-induced bidirectional stepping by dynein in which the motor moves processively under the constant force of an optical trap. Less force was required to induce forward than backward movement (11). More recently, Cleary et al. showed that the lifetimes of single monomeric dynein–MT bonds depend on the direction of applied force (20). These results imply that mechanical tension contributes to control of dynein motion along the MT.

Within each of its two separate heads, the actions of dynein's multiple AAA domains may also be coordinated. Most models focus exclusively on AAA1 because it is the principal site of ATP hydrolysis (4, 7, 21–25), and ATP binding to AAA1 weakens MT affinity (4, 22). However, mutations affecting ATP binding or hydrolysis at sites other than AAA1 also have marked effects on dynein–MT binding and ATPase activity (22, 23, 25, 26). Thus, dynein mechanochemistry is complex, with AAA1–4 activities linked together in one composite, convolved cycle.

Significance

Cytoplasmic dynein is the primary minus-end–directed microtubule (MT) motor. It is unclear how dynein coordinates ATP hydrolysis and MT attachment within and between its two motor domains, each containing four AAA+ ATPases (AAA: ATPase associated with various cellular activities), AAA1–4. We characterize how mechanical tension and nucleotide states of AAA1 and AAA3 regulate dynein–MT binding. Dynein binds MTs tighter when subjected to tension opposite its normal motility. ADP binding to AAA3 unexpectedly weakens MT-binding strength and reduces the bond strength anisotropy. Finally, AAA3 "gates" the activity of AAA1: ATP binding to AAA1 induces MT release only if AAA3 contains nucleotide. This work expands understanding of the role of force in dynein mechanochemistry and identifies regulatory functions of AAA3.

Fig. 1. Dynein–MT bond anisotropy. (*A*) Model for tension-based regulation of dynein stepping. Splaying of the dynein heads generates intramolecular tension. Under backward tension (front head) MT binding strength is greater, and under forward tension (rear head) it decreases. (*B*, *Left*) A polystyrene bead bearing a dynein motor is held in an optical trap as the microscope stage sweeps back and forth parallel to a MT (not to scale). (*Right*) The motor binds the MT, pulling the bead out of the trap. Force on the motor increases until the dynein–MT bond ruptures at the "unbinding force" (red arrow), here ~3 pN. (*C*) Primary and secondary unbinding events. Event 1 is a primary event, beginning from zero force. Secondary events (2 and 3) occur when the motor rebinds the MT before returning to the trap center. These events begin with preload F_{start} and unbind again at F_{end}, with force difference $\Delta F = F_{start} - F_{end}$. (*D*) Force (position) vs. time for WT dynein in the apo state. The inserted trace segment corresponds to the data for the period marked by the thick black line. Orange and blue shaded areas show periods of applied backward and forward tension, respectively (loading rate: 5.6 pN/s; $k \sim 0.07$ pN/nm, $v_{stage} \sim 80$ nm/s). (*E*) Normalized histograms of primary forward ($n = 575$) and backward ($n = 512$) unbinding forces, with mean values noted above the histograms. Tall vertical bands represent 95% CIs of the means (forward: [1.7, 1.8] pN, backward: [3.1, 3.6] pN) estimated by bootstrapping 4,000 samples. (*Inset*) ECDFs for the forward vs. backward directions. (*F*) Mean ΔF vs. F_{start} for forward (blue) and backward (orange) tension. Events grouped into 1-pN bins for F_{start}. Shaded regions: 95% CIs for the mean ΔF, estimated by bootstrapping 2,000 samples. For $F_{start} \gtrsim 10$ pN (gray shaded region), the trap stiffness is not constant (*SI Appendix, SI Text* and Fig. S4) and 20 or fewer events were recorded. For $F_{start} \leq 10$ pN, each mean ΔF was calculated from 36 to 770 measurements. (*G*) Unbinding rate vs. loading force derived from the data in *E* (see *SI Appendix, SI Text* for details). The shaded areas represent 95% CIs for the mean rates, estimated by bootstrapping 4,000 samples.

Here, we examine directly how tension affects dynein–MT binding and decipher how nucleotide states of AAA1 and AAA3 modulate dynein's MT attachment in the presence of force. Using an approach pioneered by the laboratory of Shin'ichi Ishiwata (14, 16), we use optical tweezers (Fig. 1*B*) to measure the force required to unbind single *Saccharomyces cerevisiae* dynein heads from MTs. We show that dynein attachment to MTs is stronger [i.e., greater force is required on average to rupture the bond (27)] under backward than under forward tension. Further, we provide evidence for unusual bonding characteristics. Protein–protein bonds are generally categorized as "slip" bonds (most common), which rupture more rapidly when force is applied; "catch" bonds (less common), which rupture more slowly in the presence of tension; and "ideal" bonds (uncommon), which are insensitive to mechanical stress (28–30). Under forward load, we find that dynein exhibits slip bonding. However [in contrast to reports of dynein catch bonding under backward load (31–33)], we find that dynein exhibits slip bonding (faster unbinding) for backward forces up to ~2 pN, and ideal bonding (constant, force-independent unbinding rate) for greater backward forces. We term this behavior "slip–ideal" bonding. Finally, we dissect AAA1- and AAA3-mediated nucleotide-induced modulation of dynein's inherent response to force, identifying (*i*) a previously undescribed weakening of MT attachment caused by ADP binding at AAA3 and (*ii*) a novel function for the linker in the AAA3-mediated "gating" of the nucleotide-dependent regulation of dynein–MT binding by AAA1. When tension is absent or applied via dynein's C terminus, ATP binding to AAA1 induces MT release only if AAA3 is in the posthydrolysis state, as described recently (9, 34). However, under more physiological conditions in which tension is applied to the linker, ATP binding to AAA3 is sufficient to "open" the regulatory gate. These results provide a basis for more complete models of the dynein mechanochemical cycle.

Results

Stronger Dynein–MT Binding Under Backward Tension. We previously demonstrated bidirectional force-induced dynein stepping, with larger forces required to induce backward steps (toward the MT plus end) (11). We predicted this behavior results from intrinsic anisotropy of the dynein–MT bond. To define the intrinsic response of an individual dynein motor domain to force, we measured unbinding forces (Fig. 1*B*) of a tail-truncated, single-headed "wild-type" (WT) dynein (Dyn1$_{331kDa}$ or VY137 dynein; see *SI Appendix, SI Materials and Methods*) in the nucleotide-free (apo) state (Fig. 1 *C*–*E*), similar to Cleary et al. (20). As expected, forces required to unbind dynein monomers from MTs were significantly larger when pulling backward (Fig. 1*D*; loading rate: 5.6 pN/s). Whereas forward unbinding forces rarely exceeded 3 pN, backward unbinding forces frequently exceeded 5 pN (and rarely, beads under backward force were carried beyond the detection range of the trap, e.g., Fig. 1*D* at ~125 s).

The largest forces in both directions usually occurred after the bead repeatedly reattached to the MT before fully returning to the trap center (Fig. 1*C*). We call these "secondary" binding/unbinding events. For "primary" events, because the bead is initially positioned at the trap center, zero force is applied to the motor immediately after binding the MT ($F_{start} = 0$), whereas for secondary events $F_{start} > 0$ [referred to as a "preload" (35)]. It is difficult to compare primary and secondary unbinding forces because for a given detachment force, the history of force applied to the bond depends on F_{start}. In other words, unbinding forces must be interpreted as a function of the preload. Our initial analysis focused on primary events (zero preload).

Normalized histograms of primary unbinding forces and empirical cumulative distribution functions (ECDFs) show that, although unbinding in either direction most often occurs between 1 and 2 pN, backward unbinding forces are frequently greater (Fig. 1*E*).

Comparison of ECDFs with a two-sample Kolmogorov–Smirnov (KS) test (36) yields a P value $p_{ks} < 10^{-10}$ (null hypothesis: the histograms have identical underlying distributions) with KS statistic $D = 0.37$ (D ranges [0,1] and measures the maximal difference between two ECDFs; see ref. 36). Although the distributions are non-Gaussian, we characterize them by the mean with 95% confidence interval for convenience (1.7 [1.7, 1.8] pN forward vs. 3.3 [3.1, 3.6] pN backward) and estimate the P value for the difference of the means via bootstrapping, $p_m < 10^{-5}$ (*SI Appendix, SI Text,* Fig. S2 for summaries of data from all experiments). Interestingly, results were similar for WT dynein with GFP at the C terminus instead of the linker (*SI Appendix, SI Text* and Fig. S3*A*).

Dynein Exhibits Slip–Ideal Bonding Under Backward Load. Under backward tension, secondary binding often results in prolonged MT attachment, even with increasing force during sequential MT encounters (Fig. 1*C*). This behavior is inconsistent with slip bonding. The higher F_{start}, the more rapidly a slip bond will break, and thus the average additional force attained ΔF will monotonically decrease. Given reports that dynein catch bonds MTs (31–33) such that the unbinding rate decreases with applied force (37, 38), we wondered whether prolonged MT attachment at high force might indicate increased bond lifetime with increasing load. Thus, we reasoned that ΔF might not decrease as a function of F_{start}.

To test this hypothesis, we measured ΔF for events with similar preloads (F_{start} bin size of 1 pN) and plotted the mean ΔF vs. F_{start} (Fig. 1*F*). Within experimental uncertainty, the mean ΔF decreases monotonically under forward load (consistent with slip bonding). However, for backward load, there is not a marked decrease, i.e., the bond breaks after a similar time (proportional to ΔF), regardless of applied force. Analysis of force-dependent unbinding rates calculated from primary unbinding events (*SI Appendix, SI Text*) (39) yielded similar results: forward unbinding rate increases with increasing load (slip bonding), but backward unbinding rate increases only up to ~2 pN and remains relatively constant as greater forces are applied (slip–ideal bonding, Fig. 1*G*).

**ATP Binding to AAA1 Weakens MT Binding Under Tension.** To better understand how dynein–MT binding is regulated, we next examined how nucleotide state affects dynein's response to tension. We first added saturating ATP [1 mM, predicted to induce MT release (40)]. Both forward and backward unbinding shifted toward smaller forces (Fig. 2*A*; *SI Appendix, SI Text* and Table S1) with the most notable difference in the first 1-pN bin. Preventing ATP binding with a K/A mutation in the AAA1 Walker-A motif yielded unbinding force distributions statistically indistinguishable from the WT apo state (Figs. 1*E* and 2*B*; *SI Appendix, SI Text,* Fig. S5*A*, and Table S1). Interestingly, although apo-state behavior is similar when tension is applied via dynein's C terminus rather than the linker (Fig. 1*E*; *SI Appendix, SI Text,* Fig. S3*A*), ATP weakens the dynein–MT binding strength more in the presence of C-terminal tension (Figs. 2*A* and 3*A*).

Because ATP is known to markedly diminish dynein's affinity for MTs (e.g., ref. 40), we postulated that its relatively small effect on WT unbinding forces with linker-applied tension was due to AAA1 hydrolyzing ATP, thus preventing observation of a pure ATP-bound state (*SI Appendix, SI Text,* and Fig. S6, state 1). We therefore introduced an E/Q mutation in the AAA1 Walker B motif to prevent ATP hydrolysis by AAA1. This mutant showed markedly weaker unbinding forces (mean <1 pN) in both directions in the presence of ATP compared with the apo state (Fig. 2 *C* and *D*; *SI Appendix, SI Text,* Fig. S5*B*, and Table S1). On the other hand, in AAA3, E/Q mutation yielded unbinding-force distributions similar to WT (Fig. 2 *A* and *E*). In the backward direction, there was no significant difference between the apo and ATP states (Fig. 2*E*; *SI Appendix, SI Text,* Fig. S5*C*, and Table S1), whereas forward unbinding forces for the two states exhibited a statistically significant but small difference in the mean (apo 1.5 [1.4, 1.6] pN vs. ATP 1.3 [1.2, 1.4] pN, $p_m = 0.02$).

AAA3 Regulates ATP-Induced, AAA1-Mediated MT Release. Having determined that AAA1 mediates ATP-induced MT release, we wondered whether AAA3 regulates this process. Using a AAA1 E/Q + AAA3 E/Q double mutant in the presence of 1 mM ATP, we tested whether simultaneous ATP states in AAA1 and AAA3 resulted in different behavior from an ATP state only in AAA1. This mutant behaved similarly to AAA1 E/Q in the presence of ATP (Fig. 2 *D* and *F*; *SI Appendix, SI Text* and Table S1), with
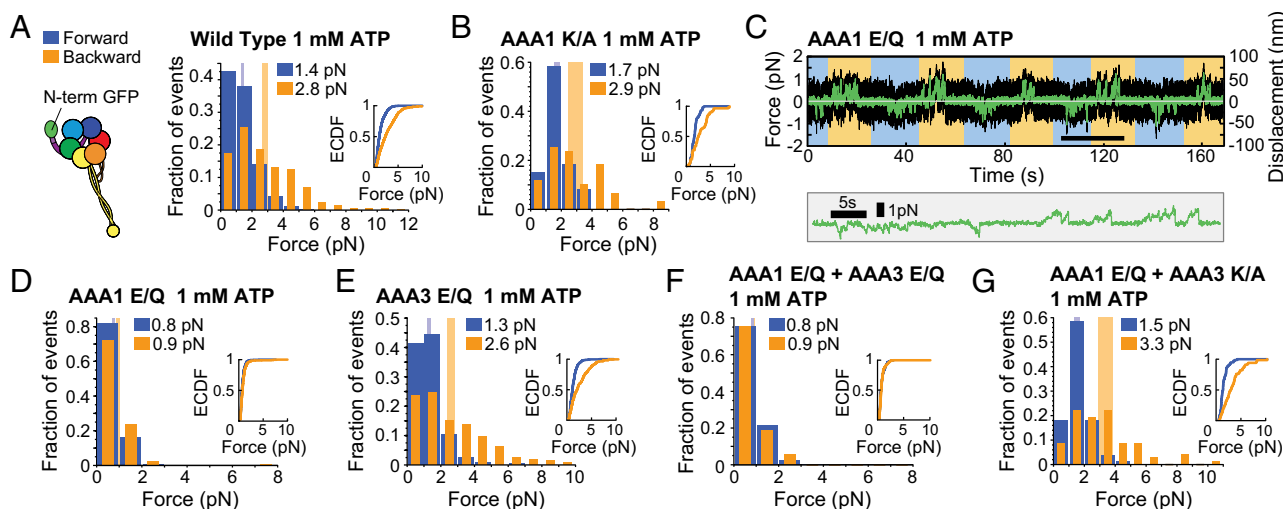
Fig. 2. Effect of 1 mM ATP on dynein's response to linker-applied tension. (*A, Left*) Schematic of dynein with GFP fused to the N terminus. (*Right*) WT dynein forward and backward unbinding forces with mean values noted. Tall vertical bands represent 95% CIs of the means (forward: [1.4, 1.5] pN, backward: [2.6, 2.9] pN) estimated by bootstrapping 4,000 samples. (*B*) As in *A*, but for the AAA1 K/A mutant (95% CIs [1.5, 1.9] and [2.5, 3.4] pN). (*C*) Example of optical trapping data for the AAA1 E/Q mutant. Black trace shows raw data. Green trace shows a fifth-order Savitzky–Golay filter with a 301-sample (0.1-s) window applied to the data to make unbinding events easier to identify. The detail shows the filtered data for the period marked by the thick black line. (*D*) As in *A*, but for the AAA1 E/Q mutant (95% CIs [0.7, 0.8] and [0.9, 1.0] pN). (*E*) As in *A*, but for the AAA3 E/Q mutant (95% CIs [1.2, 1.4] and [2.4, 2.8] pN). (*F*) As in *A*, but for the AAA1 E/Q + AAA3 E/Q mutant (95% CIs [0.8, 0.9] and [0.8, 0.9] pN). (*G*) As in *A*, but for the AAA1 E/Q + AAA3 K/A mutant (95% CIs [1.4, 1.7] and [2.9, 3.8] pN). Number of events in the forward, backward directions: (*A*) (577, 577), (*B*) (60, 59), (*D*) (320, 365), (*E*) (272, 294), (*F*) (274, 292), and (*G*) (77, 67).
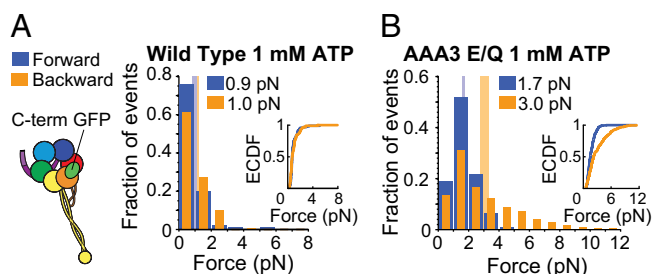
Fig. 3. Primary unbinding forces for the WT (*A*) and the AAA3 E/Q mutant (*B*) with GFP fused to the C terminus in the presence of 1 mM ATP. Tension is applied via the C terminus (loading rate: 5.6 pN/s). (*A*, *Left*) Schematic of dynein with GFP fused to the C terminus. (*Right*) Histogram of WT dynein forward (blue) and backward (orange) unbinding forces, with the respective mean values noted above each histogram. Tall vertical bands represent 95% CIs of the means (forward: [0.8, 1.1] pN, backward: [0.9, 1.2] pN) estimated by bootstrapping 4,000 samples. (*B*) As in *A*, but for the AAA3 E/Q mutant (95% CIs [1.6, 1.8] and [2.7, 3.3] pN). Number of events in the forward, backward directions: (*A*) (95, 98) and (*B*) (228, 229).

marked weakening of MT-binding strength versus the apo state (Fig. 2*F*; *SI Appendix, SI Text*, Fig. S5*D*, and Table S1). In contrast, when we prevented ATP binding to AAA3 in an AAA1 E/Q + AAA3 K/A double mutant, ATP no longer caused significant weakening of MT-binding strength (Fig. 2*G*; *SI Appendix, SI Text*, Fig. S5*E*, and Table S1) and instead yielded behavior similar to AAA1 K/A (Fig. 2*B*; *SI Appendix, SI Text* and Table S1).

The Site of Applied Tension Modifies AAA1 Gating by AAA3. As mentioned above, WT unbinding forces were markedly weakened by addition of ATP in the presence of C terminal, but not linker-applied tension. We wondered whether the site of applied tension also affects the AAA3-based gating of AAA1. Recent work by DeWitt et al. (zero-load studies and optical trapping with C-terminal tension) (34) and Bhabha et al. (zero-load studies) (9) reported similar AAA3-based regulation, but concluded that AAA3 must be in the post-ATP hydrolysis state to allow MT release. We also found that under C-terminal tension, the AAA3 E/Q mutant no longer showed ATP-induced weakened MT binding (Fig. 3 *A* and *B*; *SI Appendix, SI Text*, Fig. S3*B*, and Table S1). In addition, both the N- and C-terminal GFP-tagged AAA3 E/Q mutants showed insignificant release from MTs upon the addition of ATP in our "zero-load" MT binding and release (MTBR) assay, in contrast to the N- and C-terminal GFP-tagged WT motors (*SI Appendix, SI Text* and Fig. S7). However, under linker-applied tension, we found that ATP does weaken MT binding of the AAA3 E/Q mutant and of the AAA1 E/Q + AAA3 E/Q double mutant (Fig. 2 *A* and *D–F*).

ADP Binding to AAA1 Strengthens MT Binding, Whereas ADP Binding to AAA3 Weakens It. Having explored the response to tension and nucleotide in the apo and ATP states, we next determined the effects of ADP (*SI Appendix, SI Text* and Fig. S6, states 4 and 5). In biochemical studies, *Dictyostelium* dynein–MT affinity is the same in the apo (*SI Appendix, SI Text* and Fig. S6, state 6) and ADP states (*SI Appendix, SI Text* and Fig. S6, state 5, postpowerstroke) (40). We thus expected similar unbinding forces in apo vs. ADP states. Surprisingly, ADP (2 or 5 mM) reduced unbinding forces in both directions and minimized the intrinsic unbinding force anisotropy of the apo state (Figs. 1*E* and 4 *A* and *B*; *SI Appendix, SI Text*, Fig. S8 *A–C*, and Table S1).

To test whether the unexpected effect of ADP was due to ADP binding AAA1, we used the AAA1 K/A mutant. A total of 2 mM ADP significantly decreased unbinding forces in both directions (Figs. 4*C* and 5; *SI Appendix, SI Text*, Fig. S5*A*, and Table S1). In fact, whereas the apo state unbinding force histograms for the WT and AAA1 K/A mutants were statistically indistinguishable (*SI Appendix, SI Text* and Table S1), ADP addition to the AAA1 K/A mutant yielded mean forces even smaller than those of the WT

($p_m < 10^{-5}$ for both directions). To examine the effect of ADP binding to AAA3, we made an AAA3 K/A mutant. Apo- and (2 mM) ADP-state forward unbinding forces were statistically indistinguishable (Fig. 4*D*; *SI Appendix, SI Text*, Fig. S5*F*, and Table S1, $p_{ks} = 0.67$). Although the backward unbinding force histograms were also qualitatively similar (Fig. 4*D*; *SI Appendix, SI Text* and Fig. S5*F*), the mean backward unbinding force was greater in the ADP state (ADP 3.8 [3.5, 4.1] pN vs. apo 3.0 [2.7, 3.4] pN; *SI Appendix, SI Text* and Table S1, $p_{ks} = 0.017$, $p_m = 0.001$).

Discussion

Anisotropy of Dynein–MT Binding and the Response to Force. Our results are consistent with our own (11) and others' reports (12, 13, 20) that less force is required to break the dynein–MT bond when pulling the motor forward than backward. Interestingly, in the apo state, whether tension is applied via the linker vs. the C terminus has little effect on unbinding forces, implying that linker conformation and/or tension transmitted through the dynein ring are not responsible for the anisotropy. Cleary et al. observed similar results for a stalk/MTBD construct lacking the entire dynein ring (20). The molecular mechanism for the anisotropy remains to be elucidated and could include tension-induced reconfiguration of the coiled-coil stalk [which allosterically regulates MT affinity (5, 41, 42)], direct force-induced changes in the MTBD, geometrical reorientations of the binding interface, or even strain-induced effects on the MT lattice (43).

By deriving force-dependent detachment rates from primary unbinding forces, we found slip bonding by dynein to the MT under forward load. Under backward load, catch bonding (diminished unbinding rate with applied force) has been reported (31–33), but we instead found that slip bonding occurs up to ~2 pN, above which the unbinding rate is insensitive to force (Fig. 1 *F* and *G*), characteristic of ideal bonding (these findings agree with those from constant-force assays (20) that directly measure unbinding rates). Because the behavior seen here under rearward force exhibits features of both slip bonding (at low force) and ideal bonding (at higher force), we term it slip–ideal bonding. The
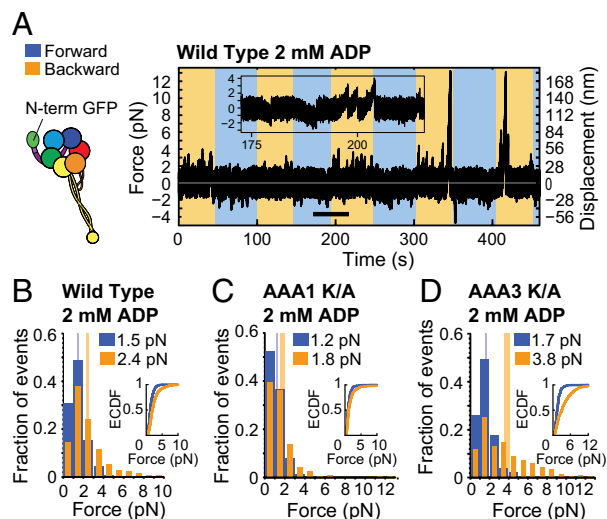
Fig. 4. Effect of ADP on dynein's response to linker-applied tension. (*A*, *Left*) Schematic of dynein with GFP fused to the N terminus. (*Right*) Optical trapping data. The inserted trace segment corresponds to data for the period marked by the thick black line. (*B*) Histogram of WT dynein forward (blue) and backward (orange) unbinding forces measured in the presence of 2 mM ADP, with the respective mean values noted above each histogram. Tall vertical bands represent 95% CIs of the means (forward: [1.4, 1.5] pN, backward: [2.3, 2.5] pN). (*C*) As in *B*, but for the AAA1 K/A mutant (95% CIs [1.1, 1.3] and [1.6, 2.0] pN). (*D*) As in *B*, but for the AAA3 K/A mutant (95% CIs [1.6, 1.8] and [3.5, 4.1] pN). Number of events in the forward, backward directions: (*B*) (996, 869), (*C*) (325, 387), and (*D*) (439, 369).
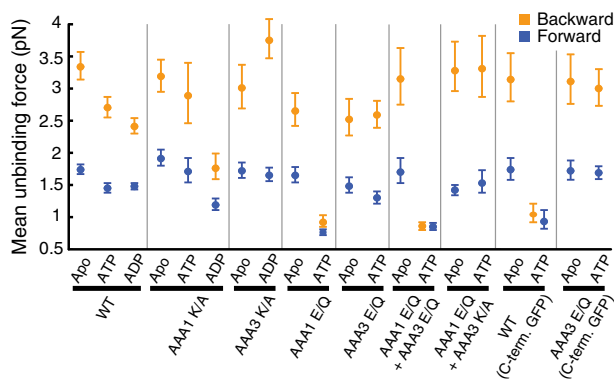
Fig. 5. Mean forward (blue) and backward (orange) unbinding forces for the various experiments reported. Error bars denote 95% CIs of the mean. The labels on the abscissa denote the experimental condition tested (*Top* row) and the constructs used (*Bottom* row).

underlying mechanism is unclear; to our knowledge this is the first report of such behavior. In a physiological context, ideal bonding may allow dynein to maintain its attachment to MTs in the presence of large opposing loads, whereas the pure slip-bonding and lesser binding strength in the forward direction may allow the motor to be pulled forward by other dyneins when working as part of a team pulling a single cargo.

Differential Effects of ADP and ATP at AAA1 and Evidence for Tension-Controlled Nucleotide Affinity. Whereas the AAA1 K/A mutant in the presence of ADP binds MTs more weakly than WT under forward and backward load (Fig. 4 *B* and *C*), the AAA3 K/A mutant binds MTs more strongly under backward load with ADP than in the apo state (Fig. 4*D*; *SI Appendix, SI Text* and Fig. S5*F*). These results suggest that, whereas ADP binding to AAA3 weakens the dynein–MT bond (discussed below), ADP at AAA1 strengthens it (consistent with the assumption that AAA1 retains ADP as dynein assumes postpowerstroke/leading/load-bearing configurations). In contrast, ATP binding to AAA1 markedly weakens MT attachment. However, whereas AAA1 E/Q exhibits weak binding in the presence of ATP, the WT shows a significant but smaller reduction in MT bond strength. Cleary et al. recently suggested that ATP has no effect on the WT dynein force-dependent unbinding rate when pulling on the linker (20). Our results generally support this conclusion (ATP weakens MT attachment substantially with tension applied via the C terminus, but not linker). However, Cleary et al. did not report unbinding rates for forces <1 pN, the force range in which greater unbinding rates would be expected, given the increased frequency of unbinding in the first 1-pN bin of our histogram (Fig. 2*A*; *SI Appendix, SI Text* and Fig. S9 *A–C*). Indeed, the WT apo and ATP unbinding rates in both directions are statistically indistinguishable for forces of 1–8 pN (*SI Appendix, SI Text* and Fig. S9*D*). Thus, for tension applied via the linker, ATP has a significant effect only for small forces ($\lesssim$1 pN).

Dynein behavior in the absence and presence of ATP could converge if tension reduces dynein's ATP affinity, explaining the similar behaviors observed for forces >1 pN (see *SI Appendix, SI Text* for detailed discussion). This would imply tension "gates" ATP binding to AAA1. Because dynein–MT binding strength is greater under backward tension, this gating mechanism would help regulate stepping by working synergistically with the intrinsic anisotropy of the dynein–MT bond strength. Backward tension on the front head leads to stronger MT binding, thereby "anchoring" the head in place. This same tension could simultaneously block ATP binding/hydrolysis in the front head until relief of intramolecular tension by release of the trailing head. Future studies should address how tension affects AAA1 ATP affinity.

Gating of AAA1-Mediated, ATP-Induced MT Release by AAA3. Although AAA3 plays an important role in controlling dynein–MT attachment (22, 23, 25), the details are just emerging. By probing dynein–MT interactions in the absence of load (9, 34) and with force applied to the dynein C terminus (34), DeWitt et al. and Bhabha et al. concluded that AAA3 must be in a posthydrolysis state for ATP-induced, AAA1-mediated MT release. Our MTBR and C-terminal pulling results support these findings, but if tension is applied via the linker, then AAA1-mediated MT release is allowed when AAA3 enters the ATP state.

It is unclear how AAA3 gates AAA1 function and how linker- vs. C-terminal tension alters this regulation. However, recent reports relate linker conformation to dynein's ATPase activities. In the absence of load, ATP at AAA3 blocks reorientation of the linker from the post- to the prepowerstroke conformation (9). In addition, binding of the cofactor Lis1, which mechanically obstructs linker movements, uncouples AAA1's ATPase activities from changes in MT-binding affinity (44). Finally, AAA5 mutations preventing linker docking severely reduce dynein's ATPase activities (3, 8). Thus, tension-induced changes in linker conformation could allosterically regulate AAA3 nucleotide state and/or AAA3–AAA1 communication, and thereby alter the effects of specific nucleotide states on AAA3-based gating of AAA1 function. This is the first evidence to our knowledge that tension applied via the linker modulates AAA3–AAA1 communication.

Weakening of MT-Binding Induced by ADP at AAA3. Somewhat unexpectedly, ADP binding to AAA3 weakens MT binding and minimizes the asymmetry between forward and backward unbinding forces (Figs. 1*E* and 4; *SI Appendix, SI Text* and Fig. S8). In the absence of force, *Dictyostelium* dynein binds MTs with essentially equal affinities in the apo and ADP states (40). However, recent yeast (apo) and *Dictyostelium* (ADP-bound) dynein crystal structures suggest that ADP release causes rearrangements within the motor domain (45). In particular, reorientations of the buttress and AAA6L/AAA5S relative to the stalk and AAA5S/AAA4S (*SI Appendix, SI Text* and Fig. S1*C*) could induce reconfigurations of the stalk and MTBD, resulting in weak MT binding. However, the apparent rearrangements could also be due to structural differences between yeast and *Dictyostelium* dynein. In addition, the AAA3 conformation itself is remarkably similar in both the apo and ADP-bound structures, raising the question of how ADP binding to AAA3 might physically exert its effects.

According to current models, the (AAA1) ADP state occurs immediately after the head steps forward, rebinds the MT, and performs the powerstroke. This configuration is expected to bear force, and thus it is surprising that MT binding would be weakened. Dynein may simply "tolerate" the moderate reduction in MT binding strength when ADP is bound. In vivo, load-sharing between groups of dyneins (46) may compensate for transiently weak attachment by single motors. Alternatively, the ADP state may be short-lived, e.g., tension could accelerate ADP release from AAA3 under physiological conditions. Even in the presence of ADP, the motor occasionally exhibits "apo-like" large secondary bindings/unbindings (Fig. 4*A*), perhaps due to ADP ejection from AAA3 when strain is applied. Unbinding assays similar to ours have shown that tension alters the affinity of myosins V and VI for ADP (18).

In the context of the mechanochemical cycle, perhaps the simplest explanation for the effects of ADP is that, unlike AAA1, AAA3 may not contain ADP following the powerstroke. AAA1 activity appears not to be strictly synchronized to that of the other AAA domains (4, 10, 25) and AAA3 hydrolyzes ATP an order of magnitude slower than AAA1 (34). Thus, AAA3 may be ADP bound only at "appropriate" points in the cycle, such as when the head is detached from the MT or when the rear head AAA1 binds ATP (thereby assisting in MT release).

Materials and Methods

Yeast Strains and Protein Purification. Engineering of yeast strains and protein purification were performed as described previously (10) with minor modifications (see *SI Appendix, SI Text*). Following initial purification, all constructs

except VY874 (AAA1 K/A), VY696 (AAA3 E/Q), and GY36 (AAA3 E/Q with a C-terminal GFP), which are insensitive to ATP-induced MT release (*SI Appendix, SI Text* and Fig. S7), were further purified by MT cosedimentation and ATP-induced release to isolate motors responsive to nucleotide. All protein was flash frozen in liquid nitrogen immediately after purification and stored at −80 °C. All motors contain an N-terminal GFP, except for VY219 (WT) and GY36, which have a GFP following the dynein C terminus. Yeast strains are listed in *SI Appendix, SI Text* and Table S2.

Unbinding-Force Measurement. MTs marked with bright fluorescent minus ends (*SI Appendix, SI Text* and Fig. S10) were covalently attached to glass coverslips of microscopy chambers as previously described (47). Anti-GFP antibody-coated, 1-μm diameter beads were then incubated with appropriate concentrations of dynein to produce MT binding by ≤50% of beads in the final assay, implying binding by single motors (48) (*SI Appendix, SI Text* and Fig. S11) for additional information). The assay buffer (11) contained 30 mM Hepes (pH 7.2), 2 mM Mg(Acetate)$_2$, and 1 mM EGTA, supplemented with 1 mg/mL β-casein, 10 μM paclitaxel, 10 mM DTT, and an oxygen scavenger system (49). Apyrase (6.6 units/mL) was added to deplete nucleotides in apo-state experiments, whereas ATP (1 mM) or ADP (2 mM, plus hexokinase) were added for experiments testing the effects of these nucleotides. Using optical tweezers described previously (50), beads were held over surface-bound MTs while the stage holding the slide chamber was swept in a triangle-wave pattern along the direction parallel to the MT long axis. The speed of movement was adjusted to produce a loading rate of 5.6 pN/s once

a motor bound. For data acquisition, signals were electronically low-pass filtered at 1.5 kHz and data were sampled at 3 kHz. See *SI Appendix, SI Text* for detailed protocols.

Data Analysis. Unbinding forces were measured using a semiautomated detection program written in MATLAB (see *SI Appendix, SI Text*). Measurements from multiple beads and experiments under the same conditions were pooled together and used to generate unbinding force histograms with 1-pN bins. The 95% confidence intervals (CIs) of the mean were calculated by bootstrapping. ECDFs for unbinding forces and KS tests to compare distributions were calculated using built-in MATLAB functions. Calculation of P values when comparing sample means was also done using bootstrapping. See *SI Appendix, SI Text* for detailed protocols.

1. Vallee RB, McKenney RJ, Ori-McKenney KM (2012) Multiple modes of cytoplasmic dynein regulation. *Nat Cell Biol* 14(3):224–230.
2. Kardon JR, Vale RD (2009) Regulators of the cytoplasmic dynein motor. *Nat Rev Mol Cell Biol* 10(12):854–865.
3. Schmidt H, Gleave ES, Carter AP (2012) Insights into dynein motor domain function from a 3.3-Å crystal structure. *Nat Struct Mol Biol* 19(5):492–497, S1.
4. Kon T, et al. (2012) The 2.8 Å crystal structure of the dynein motor domain. *Nature* 484(7394):345–350.
5. Kon T, et al. (2009) Helix sliding in the stalk coiled coil of dynein couples ATPase and microtubule binding. *Nat Struct Mol Biol* 16(3):325–333.
6. Gibbons IR, et al. (2005) The affinity of the dynein microtubule-binding domain is modulated by the conformation of its coiled-coil stalk. *J Biol Chem* 280(25):23960–23965.
7. Kon T, Mogami T, Ohkura R, Nishiura M, Sutoh K (2005) ATP hydrolysis cycle-dependent tail motions in cytoplasmic dynein. *Nat Struct Mol Biol* 12(6):513–519.
8. Toropova K, et al. (2014) Lis1 regulates dynein by sterically blocking its mechanochemical cycle. *eLife* 3:e02641.
9. Bhabha G, et al. (2014) Allosteric communication in the dynein motor domain. *Cell* 159(4):857–868.
10. Reck-Peterson SL, et al. (2006) Single-molecule analysis of dynein processivity and stepping behavior. *Cell* 126(2):335–348.
11. Gennerich A, Carter AP, Reck-Peterson SL, Vale RD (2007) Force-induced bidirectional stepping of cytoplasmic dynein. *Cell* 131(5):952–965.
12. DeWitt MA, Chang AY, Combs PA, Yildiz A (2012) Cytoplasmic dynein moves through uncoordinated stepping of the AAA+ ring domains. *Science* 335(6065):221–225.
13. Qiu W, et al. (2012) Dynein achieves processive motion using both stochastic and coordinated stepping. *Nat Struct Mol Biol* 19(2):193–200.
14. Uemura S, et al. (2002) Kinesin-microtubule binding depends on both nucleotide state and loading direction. *Proc Natl Acad Sci USA* 99(9):5977–5981.
15. Yildiz A, Tomishige M, Gennerich A, Vale RD (2008) Intramolecular strain coordinates kinesin stepping behavior along microtubules. *Cell* 134(6):1030–1041.
16. Uemura S, Ishiwata S (2003) Loading direction regulates the affinity of ADP for kinesin. *Nat Struct Biol* 10(4):308–311.
17. Gebhardt JCM, Clemen AE-M, Jaud J, Rief M (2006) Myosin-V is a mechanical ratchet. *Proc Natl Acad Sci USA* 103(23):8680–8685.
18. Oguchi Y, et al. (2008) Load-dependent ADP binding to myosins V and VI: Implications for subunit coordination and function. *Proc Natl Acad Sci USA* 105(22):7714–7719.
19. Dunn AR, Chuan P, Bryant Z, Spudich JA (2010) Contribution of the myosin VI tail domain to processive stepping and intramolecular tension sensing. *Proc Natl Acad Sci USA* 107(17):7746–7750.
20. Cleary FB, et al. (2014) Tension on the linker gates the ATP-dependent release of dynein from microtubules. *Nat Commun* 5:4587.
21. Gibbons IR, et al. (1987) Photosensitized cleavage of dynein heavy chains. Cleavage at the "V1 site" by irradiation at 365 nm in the presence of ATP and vanadate. *J Biol Chem* 262(6):2780–2786.
22. Silvanovich A, Li MG, Serr M, Mische S, Hays TS (2003) The third P-loop domain in cytoplasmic dynein heavy chain is essential for dynein motor function and ATP-sensitive microtubule binding. *Mol Biol Cell* 14(4):1355–1365.
23. Kon T, Nishiura M, Ohkura R, Toyoshima YY, Sutoh K (2004) Distinct functions of nucleotide-binding/hydrolysis sites in the four AAA modules of cytoplasmic dynein. *Biochemistry* 43(35):11266–11274.
24. Takahashi Y, Edamatsu M, Toyoshima YY (2004) Multiple ATP-hydrolyzing sites that potentially function in cytoplasmic dynein. *Proc Natl Acad Sci USA* 101(35):12865–12869.
25. Cho C, Reck-Peterson SL, Vale RD (2008) Regulatory ATPase sites of cytoplasmic dynein affect processivity and force generation. *J Biol Chem* 283(38):25839–25845.
26. Reck-Peterson SL, Vale RD (2004) Molecular dissection of the roles of nucleotide binding and hydrolysis in dynein's AAA domains in Saccharomyces cerevisiae. *Proc Natl Acad Sci USA* 101(6):1491–1495.
27. Evans E, Ritchie K (1997) Dynamic strength of molecular adhesion bonds. *Biophys J* 72(4):1541–1555.
28. Rakshit S, Zhang Y, Manibog K, Shafraz O, Sivasankar S (2012) Ideal, catch, and slip bonds in cadherin adhesion. *Proc Natl Acad Sci USA* 109(46):18815–18820.
29. Dembo M (1994) On peeling an adherent cell from a surface. *Lectures on Mathematics in the Life Sciences, Some Mathematical Problems in Biology* (American Mathematical Society, Providence, RI) Vol 24, pp 51–77.
30. Evans E (2001) Probing the relation between force—lifetime—and chemistry in single molecular bonds. *Annu Rev Biophys Biomol Struct* 30:105–128.
31. Kunwar A, et al. (2011) Mechanical stochastic tug-of-war models cannot explain bidirectional lipid-droplet transport. *Proc Natl Acad Sci USA* 108(47):18960–18965.
32. Leidel C, Longoria RA, Gutierrez FM, Shubeita GT (2012) Measuring molecular motor forces in vivo: Implications for tug-of-war models of bidirectional transport. *Biophys J* 103(3):492–500.
33. Rai AK, Rai A, Ramaiya AJ, Jha R, Mallik R (2013) Molecular adaptations allow dynein to generate large collective forces inside cells. *Cell* 152(1-2):172–182.
34. DeWitt MA, Cypranowska CA, Cleary FB, Belyy V, Yildiz A (2015) The AAA3 domain of cytoplasmic dynein acts as a switch to facilitate microtubule release. *Nat Struct Mol Biol* 22(1):73–80.
35. Yakovenko O, et al. (2008) FimH forms catch bonds that are enhanced by mechanical force due to allosteric regulation. *J Biol Chem* 283(17):11596–11605.
36. Conover WJ (1999) *Practical Nonparametric Statistics* (Wiley, New York), 3rd Ed.
37. Thomas W (2008) Catch bonds in adhesion. *Annu Rev Biomed Eng* 10:39–57.
38. Thomas WE, Vogel V, Sokurenko E (2008) Biophysics of catch bonds. *Annu Rev Biophys* 37:399–416.
39. Dudko OK, Hummer G, Szabo A (2008) Theory, analysis, and interpretation of single-molecule force spectroscopy experiments. *Proc Natl Acad Sci USA* 105(41):15755–15760.
40. Imamula K, Kon T, Ohkura R, Sutoh K (2007) The coordination of cyclic microtubule association/dissociation and tail swing of cytoplasmic dynein. *Proc Natl Acad Sci USA* 104(41):16134–16139.
41. Carter AP, et al. (2008) Structure and functional role of dynein's microtubule-binding domain. *Science* 322(5908):1691–1695.
42. Redwine WB, et al. (2012) Structural basis for microtubule binding and release by dynein. *Science* 337(6101):1532–1536.
43. Krebs A, Goldie KN, Hoenger A (2004) Complex formation with kinesin motor domains affects the structure of microtubules. *J Mol Biol* 335(1):139–153.
44. Huang J, Roberts AJ, Leschziner AE, Reck-Peterson SL (2012) Lis1 acts as a "clutch" between the ATPase and microtubule-binding domains of the dynein motor. *Cell* 150(5):975–986.
45. Carter AP (2013) Crystal clear insights into how the dynein motor moves. *J Cell Sci* 126(Pt 3):705–713.
46. Holzbaur ELF, Goldman YE (2010) Coordination of molecular motors: From in vitro assays to intracellular dynamics. *Curr Opin Cell Biol* 22(1):4–13.
47. Nicholas MP, Rao L, Gennerich A (2014) Covalent immobilization of microtubules on glass surfaces for molecular motor force measurements and other single-molecule assays. *Methods Mol Biol* 1136:137–169.
48. Gutiérrez-Medina B, Fehr AN, Block SM (2009) Direct measurements of kinesin torsional properties reveal flexible domains and occasional stalk reversals during stepping. *Proc Natl Acad Sci USA* 106(40):17007–17012.
49. Swoboda M, et al. (2012) Enzymatic oxygen scavenging for photostability without pH drop in single-molecule experiments. *ACS Nano* 6(7):6364–6369.
50. Nicholas MP, Rao L, Gennerich A (2014) An improved optical tweezers assay for measuring the force generation of single kinesin molecules. *Methods Mol Biol* 1136:171–246.

Supporting Information (SI)

SI Extended Discussion and Computational Results

Effect of tension on nucleotide affinity

We show that the AAA1 E/Q mutant exhibits weak binding in the presence of ATP (Fig. 2D), while the WT motor shows a significant but smaller reduction in MT-bond strength (Figs. 1E and 2A). This result may have important implications for the effects of tension on the AAA1 ATPase cycle.

The rate-limiting transition in the AAA1 ATPase cycle is the powerstroke (transition from the 'high-energy ADP state' to the 'low-energy ADP state' (*1*)). Thus, the majority of WT binding/unbinding events observed in the presence of ATP are likely to begin during the pre-powerstroke, high-energy ADP-state immediately following ATP hydrolysis and phosphate release (Fig. S6, state 4). MT binding stimulates the transition from the high-energy to the low-energy ADP state (ref. (*1*) and references therein), and in this state, dynein binds MTs with a greater strength than in a "true" AAA1 ATP state (as observed in the AAA1 E/Q mutant). Nevertheless, one would expect that during each MT encounter, AAA1 could progress through its cycle and enter the ATP state or any other weak MT-binding state (single unbinding events often last for several seconds, while dimeric yeast dynein displays a maximal ATPase rate k_{cat} of 16/s (*2*)). Why does this not result in markedly reduced unbinding forces?

We speculate that tension transmitted via the linker to AAA1 inhibits progression through the ATPase cycle and/or reduces AAA1 affinity for nucleotide by distorting the active site. Schmidt et al. (*3*) previously suggested that linker movements alter the size of the gap between AAA1 and AAA2, thereby modulating nucleotide affinity for the AAA1

1

binding site. In the presence of saturating ATP, WT dynein most frequently binds the MT with AAA1 in the high-energy ADP state, which is immediately followed by the strong-MT-binding low-energy ADP state (see above). Tension (particularly backward) could therefore rapidly develop, deforming the AAA1 active site and thereby either increasing nucleotide affinity (preventing release of ADP) or decreasing it (forcing ADP ejection and preventing ATP from subsequently binding). In either case, this would "lock" dynein in a strong-MT-binding state, unable to progress through its mechanochemical cycle. This cycle of tension development and inhibition of the ATP state in AAA1 would thus lead to larger unbinding forces similar to those seen in the apo state. Assuming this to be true, the slight increase in the proportion of weak unbinding forces for the WT motor in the presence of ATP (Fig. 2A) could be explained by some dynein MT-binding events occurring during the fraction of the cycle in which AAA1 has ATP bound but has not yet hydrolyzed it (similar to the weak-binding state observed for the AAA1 E/Q mutant in the presence of ATP; this effect is prevented by inhibition of ATP binding via AAA1 K/A mutation [Fig. 2B]).

In contrast to the WT motor, the AAA1 E/Q mutant experiences a constant weak MT-binding strength in the presence of ATP. The positive feedback described above would therefore never begin, because the MT bond would rupture before any significant tension developed. It is noteworthy that when applying tension via the C-terminus, MT-binding strength is decreased in the presence of ATP (also observed by Cleary et al. (4)). Thus, if tension affects AAA1 activity and/or ATP binding as described above, these effects are mediated specifically by pulling on the linker. This is consistent with the

2

hypothesis that linker tension distorts AAA1, while C-terminal tension affects other regions.

Computational validation of the Dudko method

To convert the unbinding-force histograms of the primary unbinding events in Fig. 1E into a force-dependent unbinding rate, we applied a method proposed by Dudko et al. (*5*). Specifically, we first determined the force-dependent lifetime, $\tau(F)$, as given by equation 10 in the method section of Dudko et al. (*5*) and then calculated the inverse of the lifetime to obtain the unbinding rate. To estimate the confidence intervals for the unbinding rate, we determined the confidence intervals for the counts in each bin of the histograms by using the MATLAB bootstrapping function bootci() with a sample size of 4,000. This way, we obtained two additional histograms, which represent the boundaries of the confidence intervals. We then normalized these histograms and determined the corresponding force-dependent unbinding rates, which yielded the estimates for the confidence intervals. Since the analysis proposed by Dudko et al. (*5*) is very sensitive to poor statistics in the tails of the distributions, we only display values for forces smaller than 5 pN in the forward direction and forces smaller than 9 pN in the backward direction (Fig. 1G).

To validate the use of the Dudko method (developed for transforming rupture-force histograms without "the need to make model-dependent assumptions about the functional form of $\tau(F)$" (*5*)) for the transformation of rupture-force histograms obtained from the rupture of complex bonds (such as slip-ideal and catch bonds) into force-dependent unbinding rates, we performed stochastic computer simulations. Inspired by the analytical catch-bond model by Evans et al. (*6*), we use simple Markov models with force-dependent rates to describe the behavior of a bond. The model consists of two

3

filament-bound states ("1" and "2") and one unbound state ("0"). We denote the rates for the transitions from state 1 to state 2 and from state 2 to state 1 as k_{12} and k_{21}, respectively. The rates of detachment from state 1 and state 2 (transitions to state 0) are given by k_{10} and k_{20}, respectively. To follow Kramer's theory for reaction rates (7), we allow all rates to be force dependent, with $k_{ij}(F) = k_{ij}^0 \exp(F/F_{ij})$, where F_{ij} are the force scales. For the three models tested below, we chose the intramolecular transition rates, k_{12} and k_{21}, to be large compared to all other rates (the time scale to reach an equilibration of the intramolecular states is expected to be significantly shorter than the force-dependent unbinding rate and the time scale of the experiment (8)) such that the separation of time scales introduced by Evans et al. holds and that the analytical solution for the unbinding rate as a function of force is given by (6):

$$\epsilon(F) = \frac{k_{21}(F)k_{10}(F) + k_{12}(F)k_{20}}{k_{21}(F) + k_{12}(F)}.$$

To compare this exact unbinding rate to unbinding rate data obtained by the application of the Dudko method, we performed stochastic computer simulations to generate rupture-force distributions for a slip bond, a slip-ideal bond (similar to the measured experimental backward unbinding-force distribution in Fig. 1E), and a catch-slip bond, respectively.

In our discrete-time Monte-Carlo simulations, the system starts in state 1 and after each time step, $\Delta t = 10^{-8}$ s, the force is increased by $F = F_r \Delta t$, where F_r is the loading rate. Accordingly, all rates are adjusted to the new force. The next transition of the system is chosen by comparing a uniformly distributed random number to the probabilities of possible transitions of the system (the probability of the system to change from state i to j is given by $k_{ij}(F)\Delta t$). After the transition to state 0 (bond rupture), the unbinding force is recorded and the system is set to its initial values (note that the rupture force distribution

is independent of the initial starting state since we assumed that the intramolecular bond

dynamics are fast).

From the simulations described above, we determine a rupture-force histogram

with N bins of height h_i centered at F_i. Applying the Dudko method to the generated

histogram yields the unbinding rate

$$\epsilon(F_i) = \frac{F_r h_i}{\left(\frac{h_i}{2} + \Sigma_{k=i+1}^{N} h_k\right) \Delta F},$$

where ΔF is the force difference between two adjacent bins and F_r the loading rate (5).

Using this approach, we model three different bonds, a slip bond, a slip-ideal

bond, and a catch-slip bond. To describe a slip bond, we chose $k_{12} = 0$ and $k_{10}(F) =$

$1.06\exp(F/1.746)$s^{-1}, and simulate 575 unbinding events with a loading rate of 5.6 pN/s,

as in our experiment. As expected for a slip bond, the analytical unbinding rate is in good

agreement with the force-dependent unbinding rate obtained using the Dudko method

(Fig. S12A; note that the increasing deviation for forces larger than ~4 pN is a result of

the limited number of samples in the tail of the rupture-force distribution). To simulate

slip-ideal bond behavior (as suggested by the backward unbinding-rate data in Fig. 1G),

we chose $k_{12} = 18\exp(F/0.422)$s^{-1}, $k_{21} = 100$ s^{-1}, $k_{10} = 0$ and $k_{20} = 2.21$ s^{-1}. To reproduce

the same statistics as for our experimental data (Fig. 1E, backward unbinding forces), we

simulated 512 unbinding events and used again the same loading rate as in our

experiments (5.6 pN/s). The good agreement between the analytical equation and the

force-dependent unbinding rate obtained using the Dudko method (Fig. S12B) justifies

the use of the Dudko formalism for the transformation of our backward unbinding-force

histogram into force-dependent unbinding rates (Fig. 1G; note that the limited number of

data points in the low-force regime results in the slight deviation from the analytical

equation at forces below ~2 pN, see Fig. S12B). Finally, we test the applicability of the

Dudko method to transform an unbinding-force histogram obtained from a catch-slip

bond. To simulate the characteristics of a catch-slip bond (decreasing unbinding rate with

initial application of small forces, followed by an increasing unbinding rate with further

increasing force), we chose $k_{12} = 100\exp(F/0.5)\text{s}^{-1}$, $k_{21} = 100 \text{ s}^{-1}$, $k_{10} = 0.7\exp(F/0.8)\text{s}^{-1}$,

and $k_{20} = 0.1\exp(F/5) \text{ s}^{-1}$. Here, we simulated 600 rupture-force events for a loading rate

of 1 pN/s. Also in this case, the unbinding rate obtained from the Dudko method is in

good agreement with the analytical unbinding rate (Fig. S12C). In conclusion, our

computer-based analyses demonstrate that the Dudko method can be applied to more

complex bonds (in particular to the slip-ideal bond behavior observed in the WT, apo-

state backward-pulling experiments) if the time scale of the experiment (the time of how

fast one pulls on the bond) is long compared to the time scale of how fast the bond

reaches steady state. In support of this conclusion, the estimated force-dependent, apo-

state backward unbinding rates shown in Fig. 1G (slip-ideal behavior) are in excellent

agreement with the unbinding rates that the Yildiz group reported very recently using a

constant-force unbinding assay (*4*).

**Effects of AAA3 E/Q mutation under zero load: microtubule binding and release
(MTBR) experiments**

As mentioned in the main text, we observed negligible MT release in the presence of 1

mM ATP in the MTBR assay for AAA3 E/Q mutants bearing GFP tags at either the C- or

N-terminus (whereas the WT bearing tags at these positions exhibited measurable MT

release in response to ATP; Fig. S7). Thus, in the absence of load, AAA3 E/Q mutation

diminishes the response to ATP, presumably by gating the ATP-induced weakening of

MT affinity mediated by AAA1 (in agreement with previously published reports (*9, 10*)).

For completeness, we note that other theoretical explanations are also possible. For

example, AAA3 E/Q mutation could enhance basal MT affinity such that, even for an

ATP-responsive motor in the presence of ATP, MT release would be minimal at the MT

concentration used in the experiment (i.e. the MT concentration becomes saturating even

in the presence of ATP). Although the C-terminally GFP-tagged constructs do seem to

exhibit greater basal MT affinity in this assay, their behavior in the apo state on the single

molecule level (i.e. in unbinding experiments) is similar to that of the N-terminally

tagged constructs (suggesting that either the affinities are not markedly different, or that

at least the off-rates are comparable). In addition, as we will describe in future work,

mutations may induce subtle steric effects with significant consequences in ensemble

dynein-MT binding assays such as the MTBR. Nevertheless, for both N-terminally and

C-terminally GFP-labeled constructs, initial binding in the apo state is qualitatively

similar for both the respective WT and AAA3 E/Q mutants, whereas appreciable release

is seen only in the WT (we have refrained from precise quantification of binding fractions

because the intensity of the InstantBlue stain used in this assay is nonlinear with protein

concentration).

SI Materials and Methods

Generation of yeast strains

Mutant yeast strains were created by the standard PCR-mediated yeast genetic

manipulation method (*11*), which is based on the LiAc/ss carrier DNA/PEG protocol (*12*)

with uracil and 5-fluoroorotic acid (5-FOA) as selective agents (*13*). Primers for PCR

were designed using the PrimerQuest tool from Integrated DNA Technologies

(www.idtdna.com/Primerquest). DNA fragments were generated using standard PCR

protocols. Yeast strains are listed in Table S2. For each mutant, we confirmed apo-state

behavior similar to that of WT (VY137) (Figs. S3 and S5).

Yeast culture and dynein purification

Yeast culture and dynein purification were done as described previously (*2*), with minor

modifications indicated below. The yeast strain encoding tail-truncated, wild-type dynein

$Dyn1_{331kDa}$ was designed previously in Ronald Vale's lab and named "VY137" ("VY" for

"Vale yeast") and derived from a W303 parent strain (see refs. (*14, 15*) describing W303).

VY137 has the genotype *PGal:ZZ:Tev:GFP:HA:D6 MATa; his3-11,15; ura3-1; leu2-*

3,112; ade2-1; trp1-1; pep4Δ::HIS5; prb1Δ. The gene for tail-truncated yeast dynein is

called "D6" and encodes amino acids 1219-4092 of the *S. cerevisiae* Dyn1 protein

(predicted molecular weight = 331 kDa) (*2*)[*]. It is equivalent to the 380 kDa truncated

constructs from *Dictyostelium* (*1, 17-23*). It is expressed behind the inducible galactose

promoter (P_{GAL}). At the N-terminus (i.e. preceding the N-terminus of the truncated dynein

tail domain) is a ZZ-tag (ZZ, a two-domain analogue of the immunoglobulin G-binding

portion of the staphylococcal protein A (*24*)) for binding to beads coated with IgG

(immunoglobulin G) during affinity purification, a TEV (tobacco etch virus) protease

cleavage sequence, a GFP (green fluorescent protein; specifically, yeast-enhanced GFP,

yEGFP3, a GFPmut3 optimized for yeast (*25, 26*)), and a hemagglutinin (HA) tag (not

employed in this work).

---

[*] Reck-Peterson et al. (2) and Gennerich and Reck-Peterson (16) attribute the tail-truncated "D6" construct
to amino acids 1219-409<u>3</u> rather than 1219-409<u>2</u>, as here. This is not a true discrepancy, and the error in
the earlier work is probably due to the accidental inclusion of the gene's stop codon when calculating the
total number of amino acids the gene encodes.

Yeast cells were grown in galactose-containing medium (YPG: 10 g/L yeast extract, 20 g/L peptone, 2% (w/v) galactose) to a final OD_{600} between 1.5 and 2.5. After cell harvest by centrifugation, the yeast cell pellet was resuspended in 0.2 volumes of ddH_2O and flash-frozen in liquid nitrogen as small droplets. The cell pellet was stored at -80 ºC.

During purification, the frozen droplets were pulverized using a kitchen coffee grinder, followed by addition of 0.2 volumes of 5× lysis buffer (1× dynein lysis buffer: 30 mM HEPES (pH 7.2), 50 mM KAcetate, 2 mM MgAcetate, 1 mM EGTA, 10% glycerol, 1 mM DTT, 0.1 mM Mg-ATP, 0.5 mM Pefabloc, 10 ng/ml Leupeptin, 10 ng/ml Pepstatin A, 0.2% v/v Triton X-100). After cell lysis, the lysate was cleared via ultracentrifugation at 290,000 × g for 30 min. IgG sepharose beads (Amersham Pharmacia) were then added to the supernatant and incubated for 1 hr at 4 °C while rotating.

The dynein-bound IgG beads were then washed with 10 bead volumes (BV) of dynein lysis buffer, followed by 5 BV dynein lysis buffer supplemented with 250 mM KCl and 10 BV TEV protease cleavage buffer (10 mM Tris (pH 8.0), 150 mM KCl, 0.1 mM ATP, 1 mM DTT (dithiothreitol), 0.5 mM Pefabloc, 0.1% v/v Triton X-100). The beads were resuspended in an equal volume of cleavage buffer and 2% v/v TEV protease (Life Technologies) was added. The mixture was incubated at 16 ºC for 2 hrs while rotating, resulting in cleavage of IgG-bound GFP-dynein from the beads.

Beads were sedimented by centrifugation, and the GFP-dynein-containing supernatant was flash-frozen in small aliquots using liquid nitrogen. The aliquots were stored at -80 ºC until further use. The purity and quantity of purified yeast dynein were

analyzed on 4-12% Bis-Tris SDS gels (Life Technologies) with Krypton stain (Pierce), using BSA (bovine serum albumin) as protein standard.

MT binding/release purification.
To further purify dynein prior to experiments, we performed a MT binding/release procedure. Motors are incubated with MTs, to which they bind, followed by MT sedimentation by centrifugation, removal of supernatant (containing motors unable to bind MTs), resuspension and addition of ATP (to release motors responsive to nucleotide), a final sedimentation, and removal of supernatant (containing motors capable of both MT binding and release) (*17, 27*).

To 50 µL of purified dynein, 10 µL of 10 mg/mL paclitaxel-stabilized MTs were added in the presence of 10 µM paclitaxel (Sigma). This solution was then layered onto a 100-µL sucrose cushion (30 mM HEPES, 200 mM KCl, 2 mM MgCl$_2$, pH 7.4, 10% v/v glycerol, 25% w/v sucrose, 1 mM DTT, 20 µM paclitaxel) and centrifuged at 25 °C for 10 min at 60,000 × g. After discarding the supernatant, and gently rinsing the MT pellet with 100 µL of wash buffer (identical to the sucrose cushion, but without sucrose), the pellet was resuspended in 60 µL of wash buffer with 5 mM MgATP added. This MT suspension was again centrifuged (same settings as above), and the supernatant was removed, aliquotted in 2 µL volumes and flash frozen in liquid nitrogen before storage at -80 °C. Figure S7A shows SDS-PAGE analysis of the supernatants and pellets for a typical binding/release procedure.

Polarity-marked MT preparation

The direction of unbinding forces was confirmed using polarity-marked MTs, with "bright," densely fluorescence-labeled minus ends. The polarity-marked MTs were prepared following methods similar to those provided on the Mitchison laboratory website (http://mitchison.med.harvard.edu/protocols/) and the protocol by Howard and Hyman (*28*). However, paclitaxel was used instead of GMPCPP (guanylyl 5'-α,β-methylenediphosphonate, a non-hydrolyzable GTP analog) during the polymerization of microtubule seeds (MT polymerization in the presence of paclitaxel produces short MTs (*29*)).

N-Ethylmaleimide (NEM) tubulin, which inhibits MT minus-end polymerization (*30*), was prepared by dissolving bovine brain tubulin (Cytoskeleton, Inc.) to 10 mg/mL in 100 uL of BRB80 (80 mM PIPES, 2 mM $MgCl_2$, 1 mM EGTA, pH ~7) with 0.5 mM Mg-GTP. With the tubulin solution on ice, 2.1 uL of freshly prepared 50 mM NEM (Thermo Scientific) was added (1 mM NEM final), and the solution was incubated for 10 min. The reaction was then quenched with 8 mM βME (β-mercaptoethanol) for 10 min, after which the NEM-treated tubulin was aliquotted in 5-µL volumes, flash frozen, and stored at -80 °C.

Next, bright fluorescent MT "seeds" were prepared from 1.6 µL of ~18 mg/mL Cy3-labeled tubulin (ratio labeled:unlabeled = 1:2; Cy3 labeling described in detail in ref (*31*)), to which 10 µL of polymerization buffer (BRB80 supplemented with 20 µM paclitaxel/1% DMSO, 1 mM Mg-GTP, 10% glycerol) was added (yielding ~ 2 mg/mL tubulin). This mixture was flash frozen in 3 µL aliquots and stored at -80 °C. MTs were then prepared by thawing the seed mixture and allowing polymerization for 10 min at 37

°C. During this time, a mixture of one aliquot of NEM-treated tubulin was mixed with an equal volume of Cy3-labeled tubulin (~1:23 labeled:unlabeled) and kept on ice. Polymerization buffer (BRB80 supplemented with 10% glycerol and 2.5 mM Mg-GTP) was then added and the solution placed at 37 °C for 30 seconds, after which the MT seeds were added (immediately prior to adding the seeds, the seed mixture was forcefully sheared by pipetting it up and down with the pipette tip pressed firmly against the wall of the tube). The mixture was then allowed to polymerize at 37 °C for 20 min, at which point 10 μM paclitaxel was added to stabilize the MTs.

This procedure yields Cy3-labeled MTs with brightly labeled minus ends (Fig. S10, probing the MT-directionality with the strictly plus-end-directed molecular motor kinesin-1 demonstrated that the polarity marking was on the minus end in at least 98% of MTs with a single bright spot on one end; N=43). These MTs were then used immediately for experiments (polarity marking becomes unreliable after more than one day of storage due to dynamic rearrangements of MTs (*32*)).

Anti-GFP antibody purification
Antibodies were purified from rabbit serum using an affinity column bearing purified GFP with a GST (glutathione S-transferase) tag (GST-GFP).

To express GST-GFP, the plasmid encoding GST-GFP (pGEX6P1) was transformed into NEB Express competent *E. coli* cells (New England Biolabs). A single colony was inoculated in 5 ml LB medium with 100 μg/mL carbenicillin overnight at 37 °C with vigorous shaking, and then the overnight culture was inoculated into 50 mL LB medium with 50 μg/mL carbenicillin. After ~ 2 h growth at 37 °C, the 50 ml culture was added to 1 L LB medium with 50 μg/mL carbenicillin. The culture was inoculated at

37 °C with vigorous shaking for 2-3 h until OD_{595} reached ~ 0.6-0.8, then it was cooled on ice to below 20 °C. 105 μL 1 M IPTG (isopropyl β-D-1-thiogalactopyranoside) was added to the cooled cells, and the expression of GST-GFP was induced at 20 °C overnight. The cells were harvested by centrifugation at 4000× g for 15 min at 4 °C. The cell pellet was flash frozen in liquid nitrogen and stored at -80 °C.

To purify the GST-GFP, the cell pellet was thawed on ice for 15 min, and 10 mL of lysis buffer (50 mM NaH_2PO_4, 150 mM NaCl, 1 mM EDTA (ethylenediamine-tetraacetic acid), 1 mM DTT, 2 mM PMSF (phenylmethanesulfonylfluoride), with 20 mg lysozyme, pH 7.4) was added to the pellet. The solution was incubated on ice for 30 min, and then sonicated for 10 × 30 s. The cell lysate was cleared by centrifugation (21,000× g for 30 min at 4 °C). At the same time, 5 mL glutathione resin (Qiagen, 50%) was added to a column (BioRad) and washed with 10 mL wash buffer (50 mM NaH_2PO_4, 150 mM NaCl, 1 mM EDTA, 1 mM DTT, pH 7.4). The cleared lysate was flowed through the resin. The resin was then washed with 3× 10 mL wash buffer. To elute GST-GFP, elution buffer (50 mM Tris, 100 mM NaCl, 10 mM glutathione, 1 mM DTT, pH 7.5) was added 0.5 mL at a time, and 0.5 mL solution was eluted. A desalting column (Econo-Pac 10DG, BioRad) was washed with 3 × 10 mL coupling buffer (50 mM HEPES, 80 mM $CaCl_2$, 10% glycerol, pH 7.5). The most concentrated fractions from the glutathione resin elution were loaded onto the equilibrated desalting column. The protein was eluted from the desalting column by the coupling buffer.

To covalently crosslink the purified GST-GFP to an activated immunoaffinity support (Affi-Gel 10, BioRad), 5 ml of Affi-gel 10 was transferred to a clean column. After the isopropanol in the resin drained, the resin was washed 3 × 5 mL ddH_2O,

followed by 2 × 5 mL coupling buffer. The washing time was kept to a minimum. The

washed resin was transferred to a 50-mL conical tube, and purified GST-GFP was added

to the resin. The mixture was nutated at 4 °C overnight in the dark. The resin was then

loaded to a column, and washed 3 × 10 ml storage buffer (50 mM Tris, 100 mM NaCl,

0.1% sodium azide, pH 7.6). The anti-GFP antibody affinity column was generated and

stored at 4 °C.

To purify anti-GFP antibody from rabbit serum, the anti-GFP antibody affinity

column was washed with 4 × 25 mL 100 mM phosphate (pH 7.0). The serum was diluted

2× with 100 mM phosphate (pH 7.0), and flowed through the affinity column for 4 times.

The column was then washed with the following solutions (25 mL for each): 100 mM

phosphate (pH 7.0); 100 mM phosphate, and 500 mM NaCl (pH 7.0); 100 mM HEPES

(pH 8.0); 100 mM phosphate (pH 11.5); 100 mM phosphate (pH 7.0). To elute the

antibody, each time 1 ml of 100 mM phosphate (pH 2.5) was added (to denature the GFP

and thereby release the antibody), and 1 mL of solution was collected. 60 μL of 1 M

NaOH were added to each fraction to adjust the pH to 7.0 thereby restoring the native

protein structure of the antibody. The concentration of antibody was determined by

measuring absorbance at 280 nm using a Nanophotometer (NanoDrop). Fractions with

absorbance above 0.15 were pooled and concentrated with an Amicon Ultra centrifugal

100-kDa unit (Millipore). Glycerol was supplemented to the final solution (10%). The

antibody solution was then aliquotted, flash frozen, and stored at -20 °C.

Unbinding force assay preparation

Flow chambers were prepared as described previously in detail (*31, 33*). Briefly, glass

cover slips were cleaned by sonication in a 2% v/v alkaline detergent (Mucasol) followed

by extensive rinsing, oven drying, and cleaning in a plasma cleaner (Harrick). The cover slips were then aminosilanized and stored under vacuum. Flow chambers (~10 µL volume) were assembled using these cover slips, glass microscope slides, and Parafilm. After treatment with an 8% glutaraldehyde solution (Sigma) (alternatively 5 mM of disuccinimidyl glutarate (Thermo Scientific) in DMSO was used), the chambers were rinsed extensively with at least 700 µL of ddH$_2$O and dried using filtered, compressed air or vacuum. Then 20 µL of a dilute MT suspension in BRB80 (80 mM PIPES, 2 mM MgCl$_2$, and 1 mM EGTA, pH ~7) containing 10 µM paclitaxel ("BRB/Tx") was flowed into the chamber, immediately followed by washing with 40 µL of BRB/Tx. The MTs were allowed to react with the functionalized surface for 20-90 min before blocking with "dynein trapping buffer" (30 mM HEPES (pH 7.2), 2 mM MgAcetate, 1 mM EGTA) (*34*) containing 2 mg/mL β-casein (Sigma) and 10 µM paclitaxel.

Anti-GFP antibody-coated beads were prepared as described previously (*16, 33*). Antibody was obtained from the serum of rabbits immunized with GFP, as described below.

Purified dynein motors (following MT binding/release) were removed from the -80 °C freezer and stored in liquid nitrogen until immediately before use. After thawing quickly by hand, the dynein was diluted stepwise in trapping buffer containing 1 mg/mL β-casein. Then 4 µL each of the diluted motors and a 1:50 dilution of beads in trapping buffer were mixed together and incubated for 10 min on ice to allow the motors to bind to the antibodies on the beads. The motor-bearing beads were then diluted in the final assay solution (40 µL total volume) containing 1 mg/mL β-casein (preparation described in ref. (*31*)), 10 µM paclitaxel, 10 mM DTT, and an oxygen scavenger system (*35*) (22.5 mM

15

glucose, 3 U/mL pyranose oxidase (Sigma), and 90 U/mL catalase (Sigma)). For

nucleotide-free experiments, apyrase (6.6 U/mL final, Sigma) was added to deplete any

residual ATP and ADP. For experiments with ADP, hexokinase (0.25 U/µL final, Sigma)

was added to convert any residual ATP to ADP. ATP and ADP nucleotides (Sigma) were

prepared with equimolar $MgSO_4$ and adjusted to pH 7 with NaOH prior to use (*33*).

The final 40-µL assay mixture was flowed into the slide chamber (replacing the

blocking solution), and the ends of the chamber were sealed using vacuum grease before

placing the chamber on the microscope.

Unbinding-force assay

Measurements were performed with a custom-built force-fluorescence inverted

microscope described previously (*33*).

First, a surface-bound, fluorescently-labeled MT oriented parallel to the

microscope *y*-axis was identified and precisely positioned at the center of the optical trap

using the 3D-nanopositioning stage. For initial experiments, polarity-marked MTs were

used in order to assign measured forces to the forward vs. backward directions

(subsequently, the forward vs. backward determination could be made based on the

asymmetry of the forces observed). Next, a bead was trapped, and the axial (*z*) position of

the nanopositioning stage was adjusted so that the separation between the lower surface

of the bead and the cover slip was ~50 nm. Position and trap stiffness (*k*) calibrations

were done for each bead tested. The trap stiffness was calculated using both the

equipartition and power spectral density methods (*33*)[†], and the average of the two was used.

Following calibration, the bead was placed over the MT, and the nanopositioning stage was automatically swept in a triangle-wave pattern along the *y* axis. The stage velocity *v* was chosen such that the loading rate ($R_L = v \times k$) was 5.6 pN/s (unbinding forces are proportional to loading rate (*36, 37*), so that greater loading rates will subject the molecules to greater forces). The precise value of 5.6 pN/s was somewhat arbitrary, and was the result of preliminary experiments in which $k = 0.07$ pN/nm and $v = 80$ nm/s (the velocity of yeast dynein in the absence of external load (*2*)).

For beads with attached motors, binding was observed when the bead attached to the MT was displaced from the trap center, followed by unbinding and rapid movement back toward the trap center (Fig. 1B). Each bead was tested for at least 4 min. Beads for which binding/unbinding events occurred were scored as "positive" for the presence of motors, and data were saved to disk for later analysis. Bead position data were collected at a sampling rate of 3000 Hz. At least 10 beads were tested in each experiment.

Unbinding-force calculation

To ensure that the analyzed data reflected unbinding forces from single molecules, data were only analyzed from experiments for which 50% or fewer of the beads bound/unbound (*38*) (we also qualitatively confirmed that unbinding behavior – e.g. unbinding forces and the presence of secondary unbinding events – was similar at concentrations yielding 50% vs. 10-20% binding; see Fig. S11).

[†] Note that the equation for Faxén's law in ref. (33) contains a typographical error. In the numerator of the right-hand side of the equation, γ_0 should be replaced by 1.

Unbinding force data were visualized and analyzed using custom-written software programmed in MATLAB (MathWorks). To further increase efficiency of data analysis, we implemented an algorithm to detect unbinding events automatically (this automated analysis is then verified by the user, with changes or additions made as appropriate). This software (including the underlying algorithm and the GUI discussed above) will be described in detail and made available for public use in a subsequent publication. The essential function of the algorithm is to locate discontinuities in the force vs. time curve (which is noisy due to bead diffusion) for which the signal is displaced toward zero force. First, the signal is smoothed (to minimize diffusion-based noise) and differentiated with respect to time using a Savitzky-Golay filter (*39*). Unbinding events are chosen by identifying large changes in the derivative of the smoothed data, and by identifying the characteristic "N" shape of the residuals (original data minus smoothed data) at discontinuities (*40*).

Because of mechanical drift during long measurements, the baseline of the optical trapping data can drift (~10 nm at most, corresponding to ~0.7 pN for most measurements). The differences between the signal value at unbinding and the baseline value are meaningful (provided the measurements remain in the linear region of the QPD response to displacements), but the absolute value may lead to inaccurate measurement of the unbinding force. For data in which the baseline drifted, we corrected for this using an automatic baseline detection algorithm, essentially as described by Golotvin and Williams (*41*).

Data analysis

For each experimental condition tested, unbinding force data from separate experiments were pooled. Distributions were compared prior to binning of data using the nonparametric two-sample, two-sided Kolmogorov-Smirnov (KS) test (*42*), which assumes only that data are drawn from a continuous underlying distribution.

To generate histograms, forward and backward unbinding forces were separated and grouped into bins of 1 pN in width. Normalized histograms, approximating the probability density functions for unbinding at a given force, were then calculated by dividing the value of each bin by N, the total number of unbinding force measurements. We then calculated the mean of each distribution. Because the unbinding force distributions were not normally distributed, we used bootstrapping for sampling error estimation rather than the standard error of the mean. For each histogram, 95% confidence intervals (CIs) for the mean statistic were calculated using the MATLAB bootci() function (with the default bias corrected and accelerated percentile method). Empirical (Kaplan-Meier) cumulative probability distribution functions were calculated using the MATLAB function ecdf().

To estimate *p*-values when comparing means of different distributions, we first created a dataset representing the sampling distribution of the mean for each original dataset, by bootstrapping 10^5 means with the MATLAB function bootstrp(). We then subtracted these means pairwise to create a dataset representing the sampling distribution of the difference of the means. From each measurement in this dataset, we subtracted the mean difference of means, so as to shift the distribution to a mean of zero, consistent with the null hypothesis of no difference between the means of the original unbinding force distributions. The *p*-value was then calculated as the proportion of the bootstrapped mean

differences that were at least as great as difference observed between the means of the

original datasets (two tailed test). If no bootstrapped mean differences met this criterion,

p is reported as $< 10^{-5}$.

Changes in optical trap spring constant for large bead displacements

Here we explain the reasons for ignoring measurements with $F_{start} > 10$ pN in Fig. 1F. To

calculate optical trapping forces, we employ back focal plane interferometry (*33, 43-47*)

with a quadrant photodiode (QPD). The QPD signal response to bead displacement from

the trap center is nonlinear, but can be approximated well by a 3rd-order polynomial (Fig.

S4A), which can then be mathematically inverted to determine the bead position x

corresponding to a given QPD measurement during data collection. Considering the trap

as a linear spring with stiffness k, the force can then be calculated as $F = -kx$. While this

method is valid for regions near the trap center, it becomes increasingly inaccurate for

large bead displacements (Fig. S4B). This is because the QPD response signals are in fact

linear with the trapping force over a much broader region than they are with the bead

position (*48, 49*) (because the QPD signals amount to changes in photon momentum, and

therefore the force exerted on the bead (*49, 50*)). Thus, since the QPD signals themselves

are nonlinear with bead position, the trap behaves as a linear spring over only narrow

region, at which point the force is nonlinear with displacement (k decreases near the

edges of the trapping beam (*48, 49, 51, 52*)). Therefore, for large displacements (greater

than ~150 nm), the forces calculated by our standard become unacceptably inaccurate.

Figure S3B estimates discrepancy between actual and calculated forces for our trap as a

function of bead displacement, and could in principle be used to obtain more accurate

measurements. However, even if we corrected the forces measured in the outer regions of

the trap, the loading rate at which force is applied to the motor in our experiments would not be constant (again because k varies in these outer regions). Therefore, while we have plotted all measured forces in Fig. 1F, only those with $F_{start} \leq 10$ pN are both accurate and also measured with a constant loading rate.

References

1. Mogami T, Kon T, Ito K, Sutoh K (2007) Kinetic characterization of tail swing steps in the ATPase cycle of Dictyostelium cytoplasmic dynein. *J Biol Chem* 282:21639–21644.

2. Reck-Peterson SL et al. (2006) Single-molecule analysis of dynein processivity and stepping behavior. *Cell* 126:335–348.

3. Schmidt H, Gleave ES, Carter AP (2012) Insights into dynein motor domain function from a 3.3-Å crystal structure. *Nat Struct Mol Biol* 19:492–497.

4. Cleary FB, DeWitt MA, Bilyard T, Min Htet Z, Belyy V, Chan DD, Chang AY, Yildiz A (2014) Tension on the linker gates the ATP-dependent release of dynein from microtubules. *Nat Commun* 5:4587.

5. Dudko OK, Hummer G, Szabo A (2008) Theory, analysis, and interpretation of single-molecule force spectroscopy experiments. *Proc Natl Acad Sci USA* 105:15755-15760.

6. Evans E, Leung A, Heinrich V, Zhu C (2004) Mechanical switching and coupling between two dissociation pathways in a P-selectin adhesion bond. *Proc Natl Acad Sci USA* 101:11281–11286.

7. Kramers HA (1940) Brownian motion in a field of force and the diffusion model of chemical reactions. *Physica* 7:284–304.

8. Pereverzev YV, Prezhdo E, Sokurenko EV (2011) The two-pathway model of the biological catch-bond as a limit of the allosteric model. *Biophys J* 101:2026–2036.

9. DeWitt MA, Cypranowska CA, Cleary FB, Belyy V, Yildiz A (2015) The AAA3 domain of cytoplasmic dynein acts as a switch to facilitate microtubule release. *Nat Struct Mol Biol* 22:73–80.

10. Bhabha G, Cheng H-C, Zhang N, Moeller A, Liao M, Speir A, Cheng Y, Vale RD (2014) Allosteric communication in the Dynein motor domain. *Cell* 159:857–868.

11. Baudin A, Ozier-Kalogeropoulos O, Denouel A, Lacroute F, Cullin C (1993) A simple and efficient method for direct gene deletion in Saccharomyces cerevisiae. *Nucleic Acids Res* 21:3329–3330.

12. Gietz RD, Schiestl RH (2007) High-efficiency yeast transformation using the LiAc/SS carrier DNA/PEG method. *Nat Protoc* 2:31–34.

13. Boeke JD, Trueheart J, Natsoulis G, Fink GR (1987) 5-Fluoroorotic acid as a selective agent in yeast molecular genetics. *Meth Enzymol* 154:164–175.

14. Thomas BJ, Rothstein R, Elevated recombination rates in transcriptionally active DNA. *Cell* 56:619–630.

15. Rothstein R (2005) Information regarding the provenance of Saccharomyces cerevisiae strain W303 (Webpage: http://wiki.yeastgenome.org/index.php/CommunityW303.html).

16. Gennerich A, Reck-Peterson SL (2011) Probing the force generation and stepping behavior of cytoplasmic Dynein. *Methods Mol Biol* 783:63–80.

17. Nishiura M et al. (2004) A single-headed recombinant fragment of Dictyostelium cytoplasmic dynein can drive the robust sliding of microtubules. *J Biol Chem* 279:22799–22802.

18. Höök P et al. (2005) Long range allosteric control of cytoplasmic dynein ATPase activity by the stalk and C-terminal domains. *J Biol Chem* 280:33045–33054.

19. Imamula K, Kon T, Ohkura R, Sutoh K (2007) The coordination of cyclic microtubule association/dissociation and tail swing of cytoplasmic dynein. *Proc Natl Acad Sci U S A* 104:16134–16139.

20. Roberts AJ et al. (2009) AAA+ Ring and Linker Swing Mechanism in the Dynein Motor. *Cell* 136:485–495.

21. Mizuno N, Narita A, Kon T, Sutoh K, Kikkawa M (2007) Three-dimensional structure of cytoplasmic dynein bound to microtubules. *Proc Natl Acad Sci U S A* 104:20832–20837.

22. Kon T et al. (2009) Helix sliding in the stalk coiled coil of dynein couples ATPase and microtubule binding. *Nat Struct Mol Biol* 16:325–333.

23. Kon T, Mogami T, Ohkura R, Nishiura M, Sutoh K (2005) ATP hydrolysis cycle–dependent tail motions in cytoplasmic dynein. *Nat Struct Mol Biol* 12:513–519.

24. Rondahl H, Nilsson B, Holmgren E (1992) Fusions to the 5' end of a gene encoding a two-domain analogue of staphylococcal protein A. *J Biotechnol* 25:269–287.

25. Cormack BP, Valdivia RH, Falkow S (1996) FACS-optimized mutants of the green fluorescent protein (GFP). *Gene* 173:33–38.

26. Cormack BP et al. (1997) Yeast-enhanced green fluorescent protein (yEGFP): a reporter of gene expression in Candida albicans. *Microbiol Read Engl* 143 (Pt 2):303–311.

27. Toba S, Watanabe TM, Yamaguchi-Okimoto L, Toyoshima YY, Higuchi H (2006) Overlapping hand-over-hand mechanism of single molecular motility of cytoplasmic dynein. *Proc Natl Acad Sci U S A* 103:5741–5745.

28. Howard J, Hyman AA (1993) Preparation of marked microtubules for the assay of the polarity of microtubule-based motors by fluorescence microscopy. *Methods Cell Biol* 39:105–113.

29. Carlier MF, Pantaloni D (1983) Taxol effect on tubulin polymerization and associated guanosine 5′-triphosphate hydrolysis. *Biochemistry (Mosc)* 22:4814–4822.

30. Phelps KK, Walker RA (2000) NEM tubulin inhibits microtubule minus end assembly by a reversible capping mechanism. *Biochemistry (Mosc)* 39:3877–3885.

31. Nicholas MP, Rao L, Gennerich A (2014) Covalent immobilization of microtubules on glass surfaces for molecular motor force measurements and other single-molecule assays. *Methods Mol Biol* 1136:137–169.

32. Williams RC Jr, Rone LA (1989) End-to-end joining of taxol-stabilized GDP-containing microtubules. *J Biol Chem* 264:1663–1670.

33. Nicholas MP, Rao L, Gennerich A (2014) An improved optical tweezers assay for measuring the force generation of single kinesin molecules. *Methods Mol Biol* 1136:171–246.

34. Gennerich A, Carter AP, Reck-Peterson SL, Vale RD (2007) Force-Induced Bidirectional Stepping of Cytoplasmic Dynein. *Cell* 131:952–965.

35. Swoboda M et al. (2012) Enzymatic Oxygen Scavenging for Photostability without pH Drop in Single-Molecule Experiments. *ACS Nano* 6:6364–6369.

36. Evans E (2001) Probing the relation between force–lifetime–and chemistry in single molecular bonds. *Annu Rev Biophys Biomol Struct* 30:105–28.

37. Thomas W (2008) Catch Bonds in Adhesion. *Annu Rev Biomed Eng* 10:39–57.

38. Gutiérrez-Medina B, Fehr AN, Block SM (2009) Direct measurements of kinesin torsional properties reveal flexible domains and occasional stalk reversals during stepping. *Proc Natl Acad Sci* 106:17007–17012.

39. Savitzky A, Golay MJE (1964) Smoothing and Differentiation of Data by Simplified Least Squares Procedures. *Anal Chem* 36:1627–1639.

40. Ratkovic MT, Eng KH (2009) Finding Jumps in Otherwise Smooth Curves: Identifying Critical Events in Political Processes. *Polit Anal* 18:57–77.

41. Golotvin, Williams (2000) Improved baseline recognition and modeling of FT NMR spectra. *J Magn Reson* 146:122–125.

42. Conover WJ (1999) *Practical Nonparametric Statistics* (Wiley, New York). 3rd Ed.

43. Visscher K, Gross SP, Block SM (1996) Construction of multiple-beam optical traps with nanometer-resolution position sensing. *IEEE J Sel Top Quantum Electron* 2:1066–1076.

44. Allersma MW, Gittes F, deCastro MJ, Stewart RJ, Schmidt CF (1998) Two-dimensional tracking of ncd motility by back focal plane interferometry. *Biophys J* 74:1074–1085.

45. Gittes F, Schmidt CF (1998) Interference model for back-focal-plane displacement detection in optical tweezers. *Opt Lett* 23:7–9.

46. Pralle A, Prummer M, Florin EL, Stelzer EH, Hörber JK (1999) Three-dimensional high-resolution particle tracking for optical tweezers by forward scattered light. *Microsc Res Tech* 44:378–386.

47. Rohrbach A, Kress H, Stelzer EHK (2003) Three-dimensional tracking of small spheres in focused laser beams: influence of the detection angular aperture. *Opt Lett* 28:411–413.

48. Jahnel M, Behrndt M, Jannasch A, Schäffer E, Grill SW (2011) Measuring the complete force field of an optical trap. *Opt Lett* 36:1260–1262.

49. Farré A, Marsà F, Montes-Usategui M (2012) Optimized back-focal-plane interferometry directly measures forces of optically trapped particles. *Opt Express* 20:12270–12291.

50. Smith SB, Cui Y, Bustamante C (2003) Optical-trap force transducer that operates by direct measurement of light momentum. *Methods Enzymol* 361:134–162.

51. Richardson AC, Reihani SNS, Oddershede LB (2008) Non-harmonic potential of a single beam optical trap. *Opt Express* 16:15709–15717.

52. Godazgar T, Shokri R, Reihani SNS (2011) Potential mapping of optical tweezers. *Opt Lett* 36:3284–3286.

53. Reck-Peterson SL, Vale RD (2004) Molecular dissection of the roles of nucleotide binding and hydrolysis in dynein's AAA domains in Saccharomyces cerevisiae. *Proc Natl Acad Sci* 101:1491–1495.

54. Carter AP, Cho C, Jin L, Vale RD (2011) Crystal Structure of the Dynein Motor Domain. *Science* 331:1159 –1165.

55. Redwine WB et al. (2012) Structural basis for microtubule binding and release by dynein. *Science* 337:1532–1536.

56. Kon T et al. (2012) The 2.8Å crystal structure of the dynein motor domain. *Nature* 484:345–350.

57. Carter AP (2013) Crystal clear insights into how the dynein motor moves. *J Cell Sci* 126:705–713.

58. Carter AP et al. (2008) Structure and Functional Role of Dynein's Microtubule-Binding Domain. *Science* 322:1691–1695.

59. Humphrey W, Dalke A, Schulten K (1996) VMD: visual molecular dynamics. *J Mol Graph* 14:33–38, 27–28.

60. Dudko OK, Hummer G, Szabo A (2006) Intrinsic rates and activation free energies from single-molecule pulling experiments. *Phys Rev Lett* 96:108101.

Table S1. Results of statistical comparisons for various measured unbinding force histograms

Experiment 1 (pN), mean [CI]	Experiment 2 (pN), mean [CI]	D	p_{KS}	p_m
WT apo forward 1.7 [1.7, 1.8]	WT apo backward 3.3 [3.1, 3.6]	0.37	$< 10^{-10}$	$< 10^{-5}$
WT apo forward 1.7 [1.7, 1.8]	WT ATP forward 1.4 [1.4, 1.5]	0.21	$< 10^{-10}$	$<10^{-5}$
WT apo backward 3.3 [3.1, 3.6]	WT ATP backward 2.7 [2.6, 2.9]	0.11	$<$ 0.003	$<10^{-5}$
AAA1 K/A apo forward 1.9 [1.8, 2.1]	AAA1 K/A ATP forward 1.7 [1.5, 1.9]	0.11	0.49	-
AAA1 K/A apo backward 3.2 [3.0, 3.5]	AAA1 K/A ATP backward 2.9 [2.5, 3.4]	0.10	0.72	-
AAA1 E/Q apo forward 1.6 [1.5, 1.8]	AAA1 E/Q ATP forward 0.8 [0.7, 0.8]	0.56	$< 10^{-10}$	$<10^{-5}$ *
AAA1 E/Q apo backward 2.7 [2.4, 2.9]	AAA1 E/Q ATP backward 0.9 [0.9, 1.0]	0.56	$< 10^{-10}$	$<10^{-5}$ *
AAA3 E/Q apo forward 1.5 [1.4, 1.6]	AAA3 E/Q ATP forward 1.3 [1.2, 1.4]	0.15	0.01	0.02
AAA3 E/Q apo backward 2.5 [2.3, 2.8]	AAA3 E/Q ATP backward 2.6 [2.4, 2.8]	0.09	0.34	-
AAA1 E/Q + AAA3 E/Q ATP forward 0.8 [0.8, 0.9]	AAA1 E/Q ATP forward 0.8 [0.7, 0.8]	0.01	0.099	-
AAA1 E/Q + AAA3 E/Q ATP backward 0.9 [0.8, 0.9]	AAA1 E/Q ATP backward 0.9 [0.9, 1.0]	0.07	0.46	-
AAA1 E/Q + AAA3 E/Q apo forward 1.7 [1.5, 1.9]	AAA1 E/Q + AAA3 E/Q ATP forward 0.9 [0.8, 0.9]	0.53	$< 10^{-10}$	$<10^{-5}$
AAA1 E/Q + AAA3 E/Q apo backward 3.2 [2.8, 3.6]	AAA1 E/Q + AAA3 E/Q ATP backward 0.9 [0.8, 0.9]	0.65	$< 10^{-10}$	$<10^{-5}$
AAA1 E/Q + AAA3 K/A apo forward 1.4 [1.3, 1.5]	AAA1 E/Q + AAA3 K/A ATP forward 1.5 [1.4, 1.7]	0.10	0.59	-
AAA1 E/Q + AAA3 K/A apo backward 3.3 [3.0, 3.7]	AAA1 E/Q + AAA3 K/A ATP backward 3.3 [2.9, 3.8]	0.08	0.9	-
AAA1 E/Q + AAA3 K/A ATP forward 1.5 [1.4, 1.7]	AAA1 K/A ATP forward 1.7 [1.5, 1.9]	0.22	0.059	-

AAA1 E/Q + AAA3 K/A ATP backward 3.3 [2.9, 3.8]	AAA1 K/A ATP backward 2.9 [2.5, 3.4]	0.12	0.71	-
WT apo forward 1.7 [1.7, 1.8]	WT 2 mM ADP forward 1.5 [1.4, 1.5]	0.16	$<10^{-8}$	$<10^{-5}$
WT apo backward 3.3 [3.1, 3.6]	WT 2 mM ADP backward 2.4 [2.3, 2.5]	0.22	$<10^{-10}$	$<10^{-5}$
AAA1 K/A apo forward 1.9 [1.8, 2.1]	AAA1 K/A 2 mM ADP forward 1.2 [1.1, 1.3]	0.36	$<10^{-10}$	$<10^{-5}$
AAA1 K/A apo backward 3.2 [3.0, 3.5]	AAA1 K/A 2 mM ADP backward 1.8 [1.6, 2.0]	0.40	$<10^{-10}$	$<10^{-5}$
WT apo forward 1.7 [1.7, 1.8]	AAA1 K/A apo forward 1.9 [1.8, 2.1]	0.06	0.44	-
WT apo backward 3.3 [3.1, 3.6]	AAA1 K/A apo backward 3.2 [3.0, 3.5]	0.05	0.71	-
WT 2 mM ADP forward 1.5 [1.4, 1.5]	AAA1 K/A 2 mM ADP forward 1.2 [1.1, 1.3]	0.23	$<10^{-10}$	$<10^{-5}$
WT 2 mM ADP backward 2.4 [2.3, 2.5]	AAA1 K/A 2 mM ADP backward 1.8 [1.6, 2.0]	0.34	$<10^{-10}$	$<10^{-5}$
AAA3 K/A apo forward 1.7 [1.6, 1.9]	AAA3 K/A 2 mM ADP forward 1.7 [1.6, 1.8]	0.056	0.67	-
AAA3 K/A apo backward 3.0 [2.7, 3.4]	AAA3 K/A 2 mM ADP backward 3.8 [3.5, 4.1]	0.15	0.017	0.001
AAA3 E/Q C-term. GFP apo forward	AAA3 E/Q C-term. GFP ATP forward	0.08	0.65	-
AAA3 E/Q C-term. GFP apo backward	AAA3 E/Q C-term. GFP ATP backward	0.05	0.97	-

* also $p_m < 10^{-5}$ when compared to the corresponding measurement in the WT apo state

**Table S1:** Results of statistical comparisons for various measured unbinding force histograms. D is the KS test parameter. p_{ks} is the p-value for the KS test and p_m is the p-value for comparison of the means using bootstrapping (see SI methods). For comparisons in which $p_{ks} \geq 0.05$ (i.e. the two histograms are statistically indistinguishable), p_m is not calculated.

Table S2. Yeast strains used in this work

Strain	Genotype	Description
VY137	*pep4Δ::HIS3, prb1Δ, pGAL-ZZ-TEV-GFP-3×HA-331DYN1*	WT with GFP at N terminus
VY219	*pep4Δ::HIS3, prb1Δ, pGAL-ZZ-TEV-3×HA-331DYN1-GFP*	WT with GFP at C terminus
GY874	*pep4Δ::HIS3, prb1Δ, pGAL-ZZ-TEV-GFP-3×HA-331DYN1(K1802A)*	AAA1 K/A with GFP at N terminus
GY861	*pep4Δ::HIS3, prb1Δ, pGAL-ZZ-TEV-GFP-3×HA-331DYN1(K2424A)*	AAA3 K/A with GFP at N terminus
GY863	*pep4Δ::HIS3, prb1Δ, pGAL-ZZ-TEV-GFP-3×HA-331DYN1(E1849Q)*	AAA1 E/Q with GFP at N terminus
GY696	*pep4Δ::HIS3, prb1Δ, pGAL-ZZ-TEV-GFP-3×HA-331DYN1(E2488Q)*	AAA3 E/Q with GFP at N terminus
GY878	*pep4Δ::HIS3, prb1Δ, pGAL-ZZ-TEV-GFP-3×HA-331DYN1(E1849Q, E2488Q)*	AAA1 E/Q + AAA3 E/Q with GFP at N terminus
GY879	*pep4Δ::HIS3, prb1Δ, pGAL-ZZ-TEV-GFP-3×HA-331DYN1(E1849Q, K2424A)*	AAA1 E/Q + AAA3 K/A with GFP at N terminus
GY36	*pep4Δ::HIS3, prb1Δ, pGAL-ZZ-TEV-3×HA-331DYN1(E2488Q)-GFP*	AAA3 E/Q with GFP at C terminus

Table S2: Yeast strains used in this work. "331DYN1" encodes amino acids 1219-4092 of Dyn1, with predicted molecular weight of 331 kDa (see ref. (*2*) and remark in footnote on page 8, section "Yeast culture and dynein purification"), and WT ("wild type") represents the tail-truncated, single-headed dynein construct without AAA mutation.

SI Figures
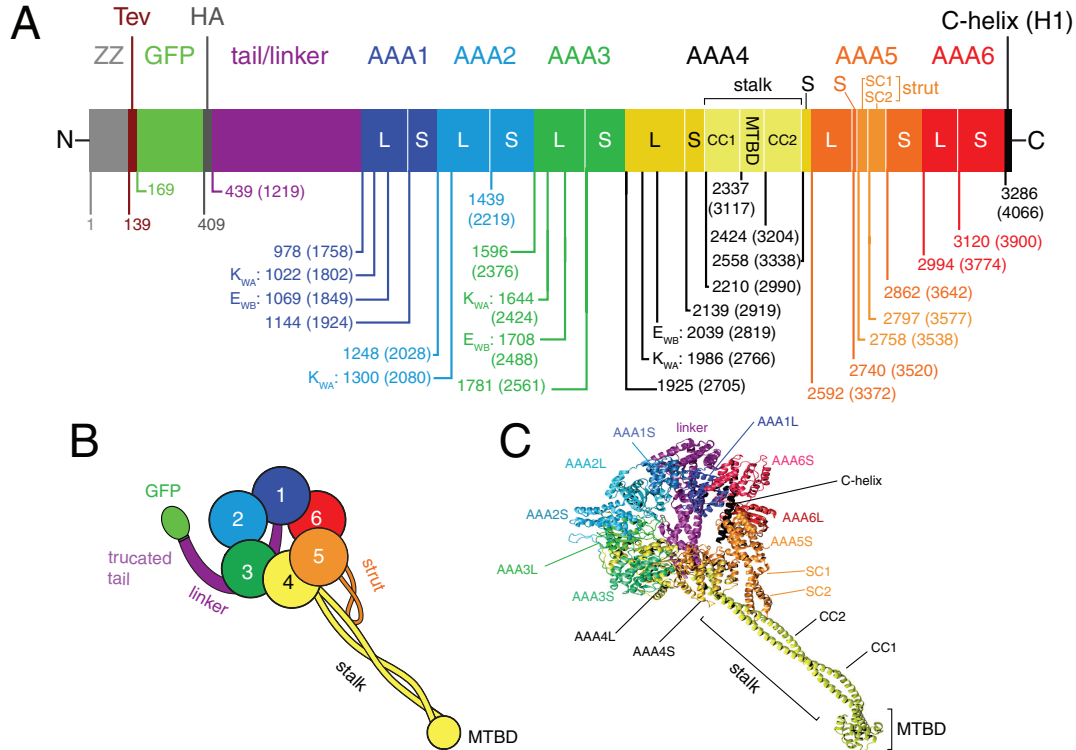
Fig. S1. Structure of VY137 monomeric dynein. (*A*) Linear map of primary structure from amino (N, left) to carboxy (C, right) termini, with color-coded regions corresponding to the different domains of the VY137 construct. The N-terminal ZZ tag (ZZ) is removed during the purification via proteolysis at the TEV cleavage site (Tev), leaving an N-terminal GFP, followed by an HA tag (unused in this work), and fused to a dynein heavy chain lacking the first 1218 amino acids of the tail. The dynein heavy chain comprises the truncated tail/linker, six AAA+ domains (AAA1-AAA6) joined by flexible linkers, and a short C-terminal helix (C-helix). Each AAA+ domain consists of a so-called "large" (L) and "small" (S) subunit (also referred to as "α/β" and "α", respectively). AAA4S contains an insertion forming the dynein "stalk", which consists of a coiled-coil with a microtubule-binding domain (MTBD) between the outgoing (CC1) and incoming (CC2) helices. AAA5S also contains an insertion comprising two helices (SC1 and SC2) that form the "strut," or "buttress." Labels below the map show the residue number corresponding to the beginning of each structural element (numbers in parentheses are the corresponding residues in full-length dynein). Divisions between domains were assigned in flexible linker regions. Lysine (K_{WA}) and glutamate (E_{WB}) residues in conserved Walker A and Walker B motifs, respectively, are also noted. Except for the noted point mutations (e.g. "AAA3 K/A" for a Walker A mutation at AAA domain 3), all constructs used here are identical to VY137, with the exception of VY219 (for which the GFP resides at the C terminus rather than preceding the linker). This map was constructed by consulting refs. (*3, 53-57*) (*B*) Schematic diagram of VY137, following cleavage of the ZZ tag, as viewed from the C-terminal face of the dynein ring. AAA+ domains are colored as in (*A*). (*C*) Cartoon of the dynein heavy chain viewed from the same orientation as in (*A*), with structures colored according to the map in (*A*). The crystal structure of the yeast motor domain (*3*) is combined with a separate structure for the mouse MTDB (*58*) via an artificial coiled-coil, as done by Carter (*57*). Small (AAA1S-AAA6S) domains are shown in lighter shades than large domains (AAA1L-AAA6L). This cartoon was prepared with VMD (*59*) using PDB entries 4AKG (motor domain), 3ERR (MTBD), and 1D7M (artificial length coiled-coil) and the Persistence of Vision Raytracer (POV-Ray, www.povray.org).

30
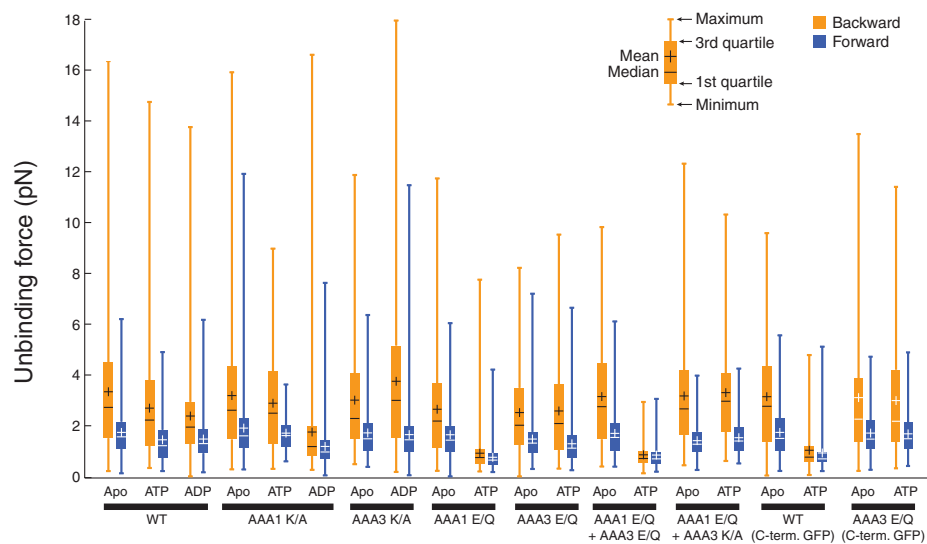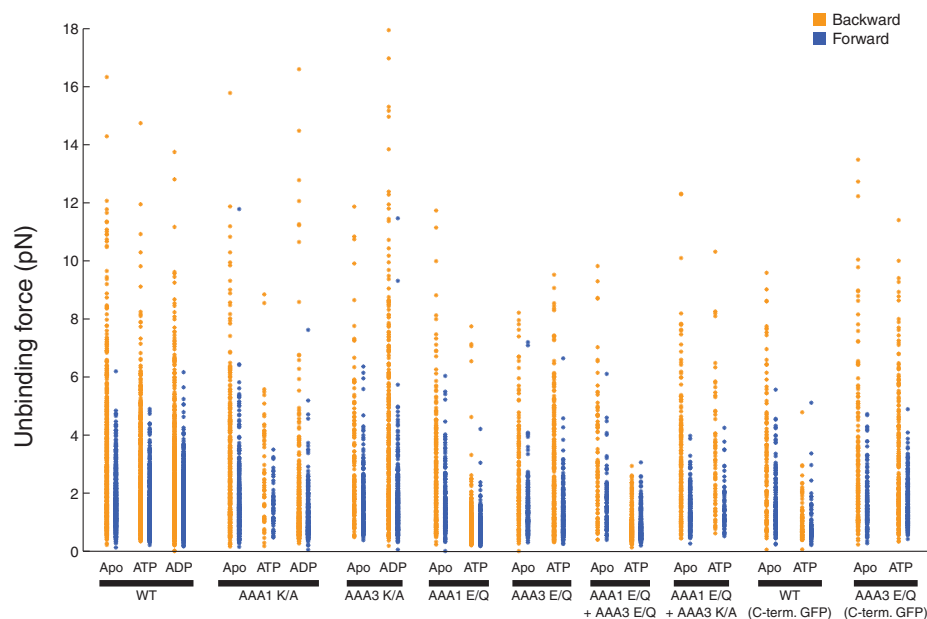
Fig. S2. Summary of unbinding force results. The labels on the abscissa denote the experimental condition tested (top row) and the construct used (bottom row; thick lines denote that the construct labeled below was used for all experiments above). (*A*) Box-and-whisker plot. The solid bars represent the interquartile range, while the whiskers denote the most extreme data in each dataset. The crosses denote the mean, while the horizontal lines indicate the median. (*B*) Vertical scatter plot. For each experiment, a single point is plotted for each data point (unbinding force) along a vertical line corresponding to the given experiment.

31
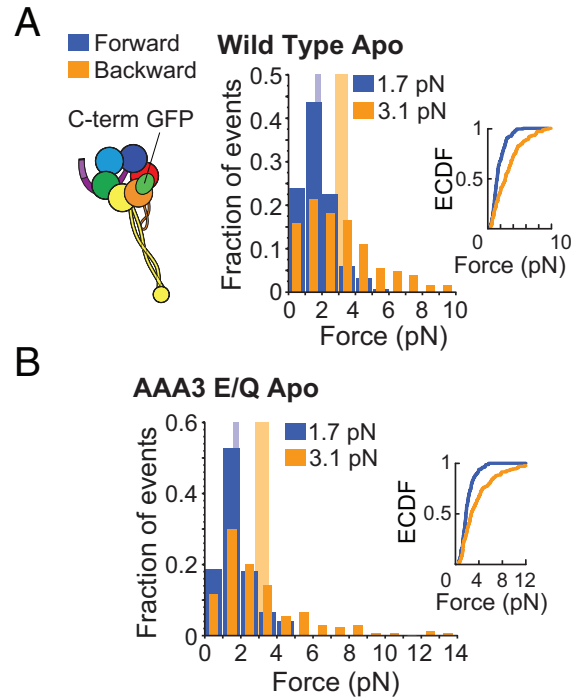
Fig. S3. Primary unbinding forces for the WT motor (*A*) and the AAA3 E/Q mutant motor (*B*) with GFP fused to the C-terminus in the absence of nucleotide (apyrase used to deplete any residual nucleotide). Tension is applied via the C-terminus rather than the linker. The loading rate was 5.6 pN/s. (*A*) *Left*: Schematic of dynein with GFP fused to the C-terminus. *Right*: Histograms of forward (blue) and backward (orange) unbinding forces, with the respective mean values noted above each histogram. Tall vertical bands represent 95% CIs of the means (forward: [1.6, 1.9] pN, backward: [2.8, 3.6] pN) estimated by bootstrapping 4,000 samples. (*B*) As in (*A*), but for the AAA3 E/Q mutant (95% CIs [1.6, 1.9] and [2.8, 3.5] pN).
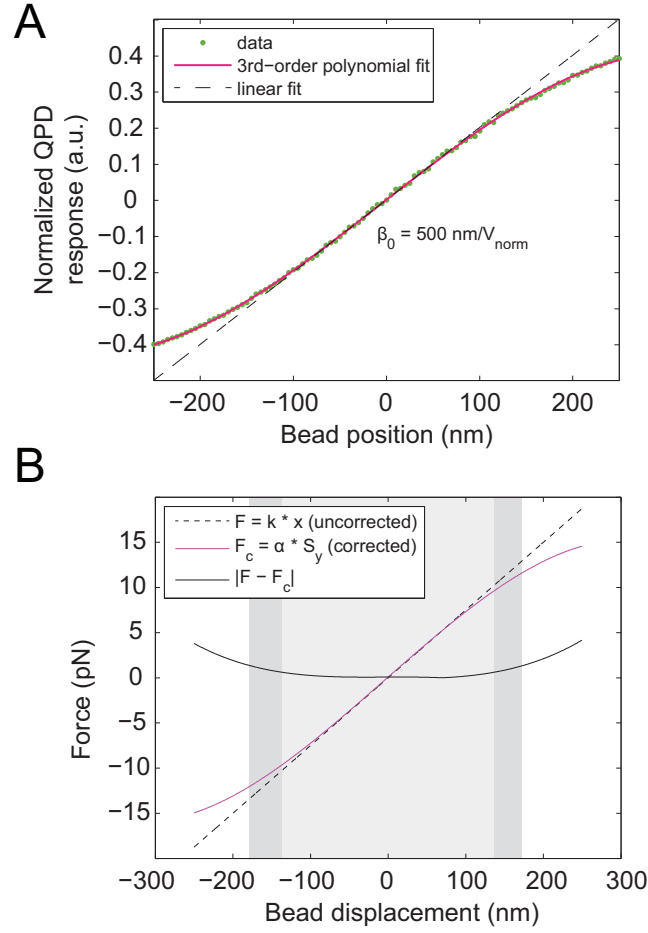
Fig. S4. Nonlinearity in optical trapping force for large bead displacements. (*A*) Green points: Normalized quadrant photodiode (QPD) response signal $S_y = (V_A + V_B - V_c - V_D)/(V_A + V_B + V_c + V_D)$, where the terms on the right hand side are the measured voltages in each of the four QPD quadrants, A, B, C, and D. Dashed line: linear fit to the ± 50 nm region. β_0 is the inverse slope of the line (V_{norm} indicates "normalized voltage"). Solid red curve: 3rd-order polynomial fit to the data. (*B*) Trapping force as a function of bead displacement for a spring constant $k_{meas} = 0.075$ pN/nm measured near the trap center. Dashed/dotted blue line: uncorrected force calculated from $F = k_{meas} x$. Solid magenta curve: corrected response, $F = \alpha S_y$, taking into account a reduced spring constant toward the edge of the trap. α is the product of $\beta(x) k(x)$, where beta is the derivative of the S_y curve, and $k(x)$ is the position-dependent spring constant. α is approximately a constant, so the value calculated near the trap center, i.e. $\alpha = \beta(0)*k(0) = \beta_0* k_{meas}$, is applicable at all positions. Dashed black line: absolute value of the error in the uncorrected force calculation. The light (dark) gray box shows the region in which the error is 5% (10%) or less of the total force, approximately [-135, 135] nm ([-175, 175] nm). The same position regions apply at different spring constants, but the corresponding force scales accordingly.

33
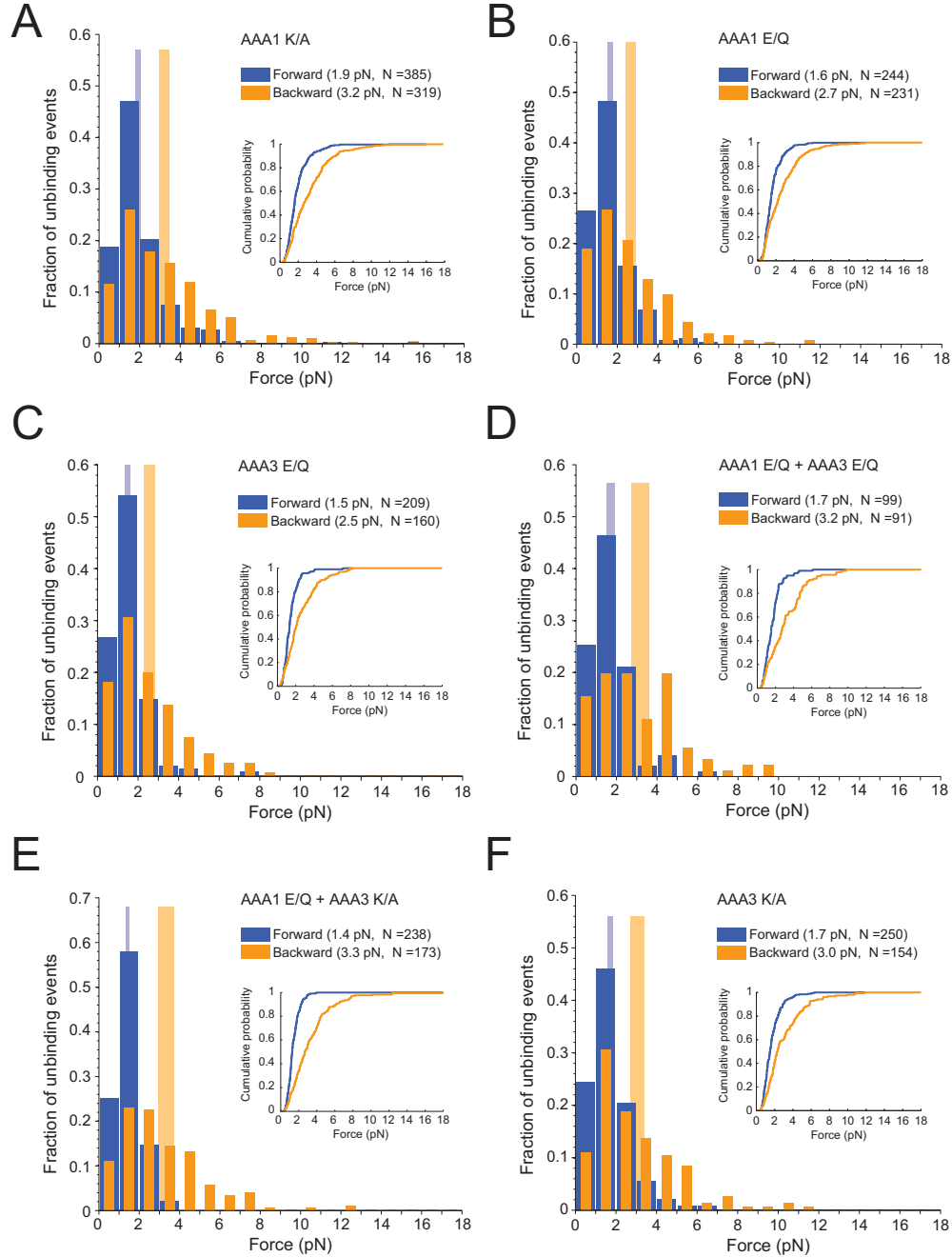
Fig. S5. Primary unbinding forces in the absence of nucleotide for nucleotide hydrolysis and binding mutants. Apyrase was used to deplete any residual nucleotide. The loading rate in all experiments was 5.6 pN/s. Forward unbinding forces are shown in blue, and backward unbinding forces are in orange. Tall vertical bands denote the 95% CIs of the mean (calculated by bootstrapping) for the forward (blue) and backward (orange) primary unbinding forces, respectively. The insets show the empirical cumulative distribution functions calculated from the measured forces (without binning). *N* is the number of total events measured in the given direction. (*A*) Nucleotide binding mutant AAA1 K/A (95% CIs [1.8, 2.1] and [3.0, 3.5] pN). (*B*) Hydrolysis mutant AAA1 E/Q (95% CIs for forward and backward directions, respectively: [1.5, 1.8] and [2.4, 2.9] pN). (*C*) Hydrolysis mutant AAA3 E/Q (95% CIs [1.4, 1.6] and [2.3, 2.8] pN). (*D*) Nucleotide hydrolysis double mutant AAA1 E/Q + AAA3 E/Q (95% CIs [1.5, 1.9] and [2.8, 3.6] pN). (*E*) Nucleotide hydrolysis/binding double mutant AAA1 E/Q + AAA3 K/A (95% CIs [1.3, 1.5] and [3.0, 3.7] pN). (*F*) Nucleotide binding mutant AAA3 K/A (95% CIs [1.6, 1.9] and [2.7, 3.4] pN).
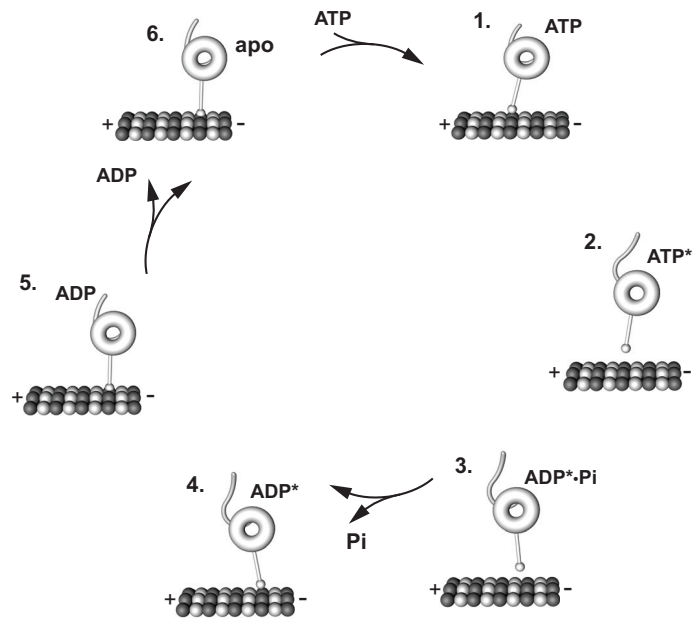
Fig. S6. Consensus model for dynein's mechanochemical cycle. ATPase states are assumed to be those in AAA1 and the other AAA sites are generally disregarded. (1, 2) ATP binding causes MT detachment and 'recocking' of the linker. (3) ATP hydrolysis in the free head. (4) Rebinding to the MT causes P_i release and induces the '*high*-energy *ADP* state*'. (5) Transition to the 'low-energy ADP state' generates a linker swing (powerstroke) toward the MT minus-end. (6) Tight MT binding in the apo (nucleotide-free) state.
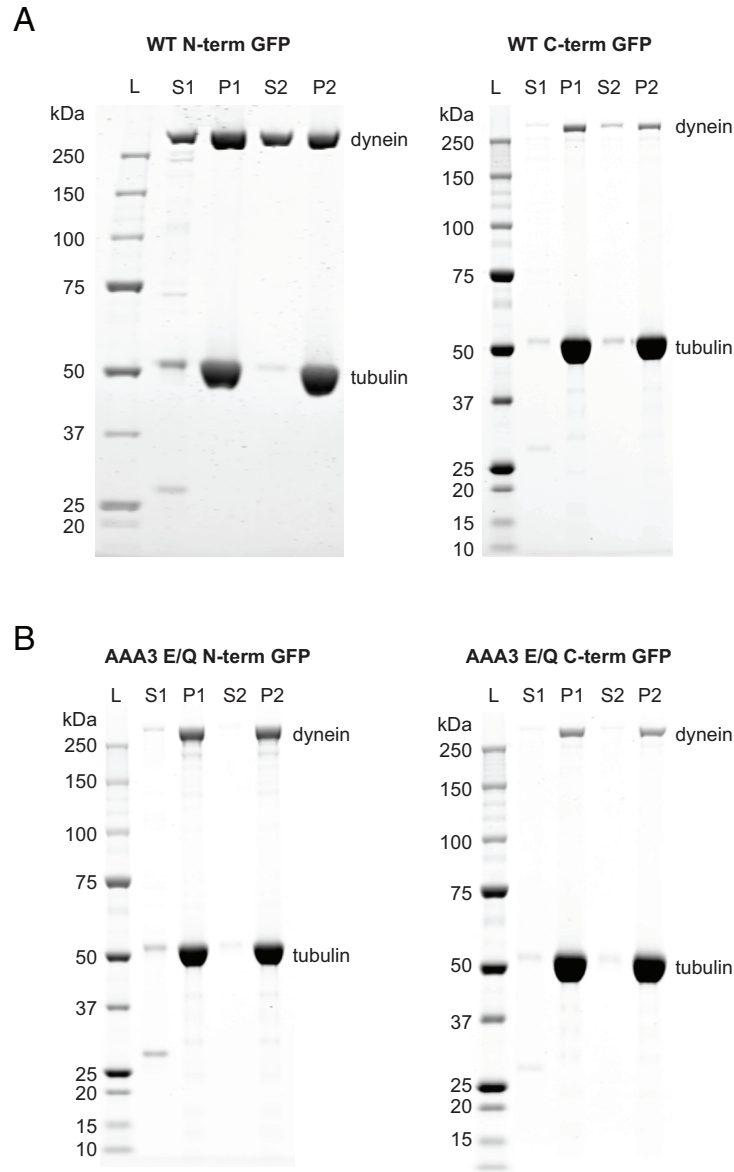
Fig. S7. MT binding/release assay (SDS-PAGE) with various single-headed dynein constructs. 5 μl samples were taken from the supernatants (S1 and S2) and re-suspended pellets (P1 and P2) at each stage of the MT binding/release assay (~ 1.7 mg/mL MTs), mixed with SDS loading buffer and denatured in boiled water for 10 min. The samples were then loaded onto a NuPAGE® Novex® 4-12% Bis-Tris Gel (Life Technologies) and ran for 50 min at 200 V in MOPS SDS running buffer (Life Technologies). The gel was then rinsed with ddH$_2$O and stained with InstantBlue™ (Expedeon) for 30 min. The high-molecular weight band is single-headed dynein, and the lower ~50-kDa band is tubulin. After the first sedimentation, there is some dynein in the supernatant (S1), but most is bound to MTs in the pellet (P1). Some tubulin is present in S1, likely small MTs or unpolymerized MT subunits. After resuspension of the pellet (P1) with ATP-containing buffer, followed by re-sedimentation, a significant fraction of dynein is present in the supernatant (S2) for WTdynein with N-terminal GFP or C-terminal GFP (*A*), while AAA3 E/Q mutants with N-terminal GFP or C-terminal GFP are almost undetectable in the supernatant (*B*). The lowest ~27K band in the S1 lanes is AcTEV™ Protease (Life Technologies) used during the dynein purification procedure.
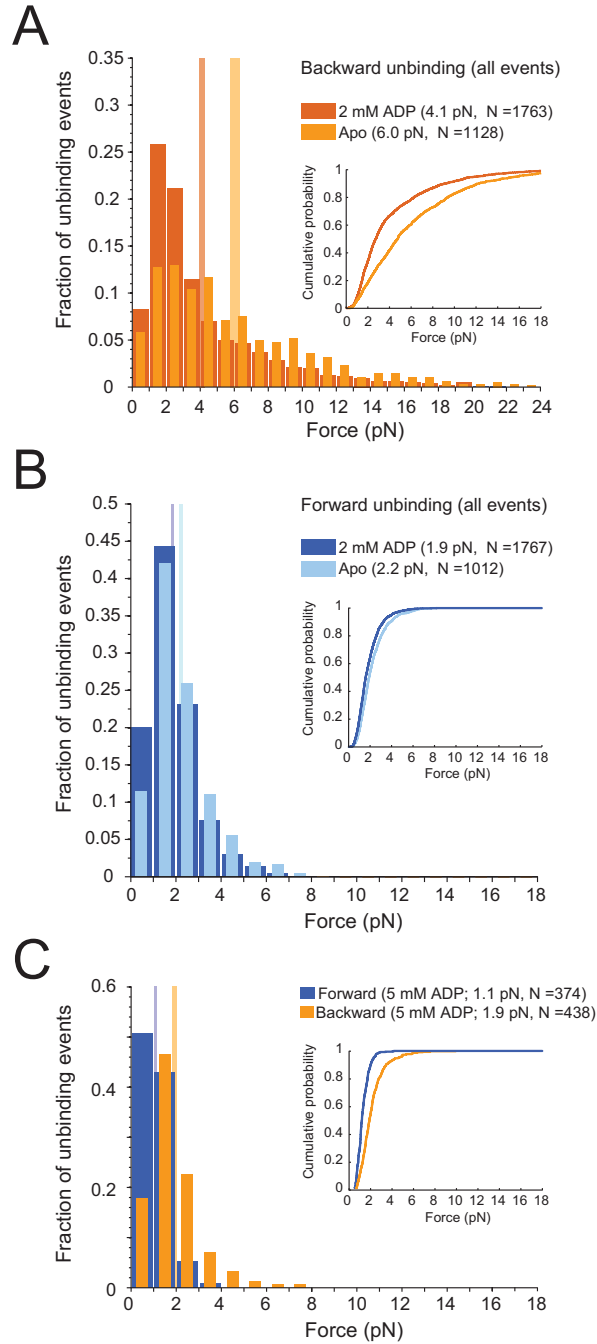
Fig. S8. Comparison of primary and secondary backward (*A*) and forward (*B*) unbinding forces for the WT motor domain in the presence of 2 mM ADP and in the absence of nucleotide, respectively, and effect of 5 mM ADP on dynein's response to tension (*C*). The loading rate was 5.6 pN/s. Tal vertical bands denote the 95% CIs of the mean (calculated by bootstrapping) for the 2 mM ADP (95% CIs for backward and forward unbinding forces, respectively: [3.9, 4.3] and [1.8, 1.9] pN), Apo (95% CIs for backward and forward unbinding forces, respectively: [5.8, 6.3] and [2.1, 2.3] pN), and 5 mM ADP (95% CIs for backward and forward unbinding forces, respectively: [1.8, 2.1] and [1.1, 1.2] pN) experiments, respectively. *N* is the number of total events measured in the given direction. The insets show the empirical cumulative distribution functions calculated from the measured forces (without binning).
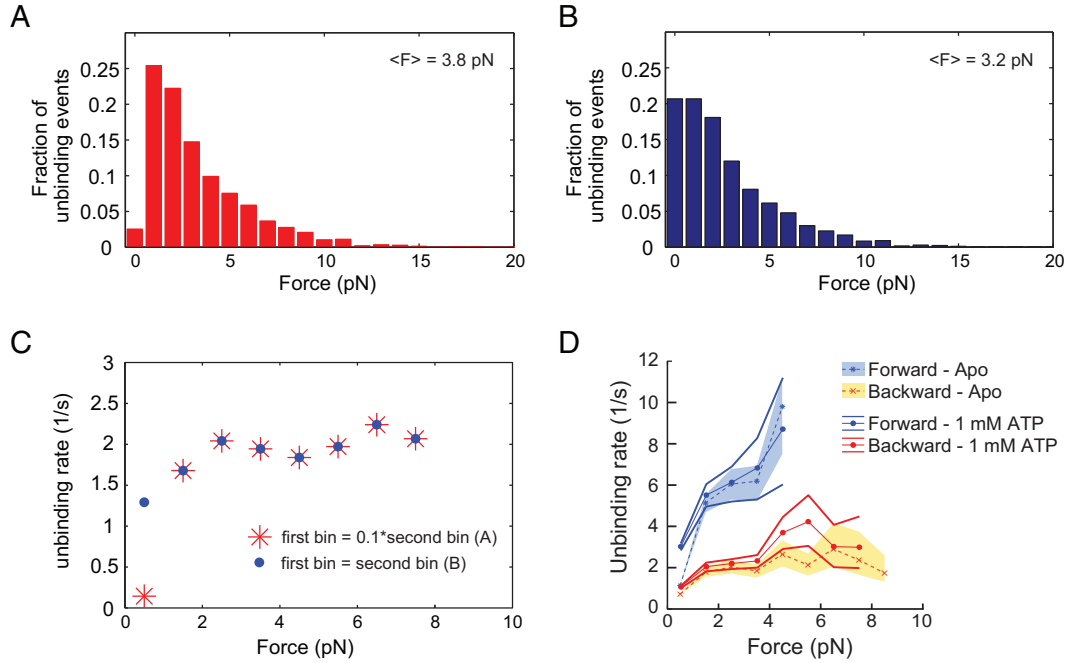
Fig. S9. Effect of changing the first 1-pN bin of a rupture-force distribution on the estimated force-dependent unbinding rates, and calculated Apo and ATP unbinding rates for the WT motor. (*A*) Rupture-force distribution in which the height of the first bin is 1/10 of the height of the second bin. (*B*) Rupture-force distribution in which the first and the second bin have the same height. The relative heights of the other bins are the same as in the distribution shown in (*A*). Because of this increased population of small unbinding forces, the corresponding average force is smaller compared to the average force of the distribution in (A). (*C*) Corresponding unbinding rates as a function of force calculated with the Dudko-method for the distributions shown in (*A*) and (*B*). The difference in the distributions is only reflected at the first data point. (*D*) Unbinding rate vs. loading force obtained from analyzing the unbinding-force distributions of the primary unbinding events shown in Fig. 1E (Apo) and Fig. 2A (1 mM ATP). The shaded areas (Apo) and the thick lines (1 mM ATP) represent 95% confidence intervals for the mean values, estimated by bootstrapping 4,000 samples. While a KS test rejects the null hypothesis that the apo and ATP forward unbinding rate data are drawn from identical underlying distributions (p<10^{-16}, D = 0.25), when excluding unbinding rates measured below 1 pN, KS analysis suggests that the forward unbinding rate data are statistically indistinguishable (*p*=0.09, D=0.09). Applying a KS test to the apo and ATP backward unbinding rate data for all rates measured below 8 pN suggests that the distributions are statistically indistinguishable (*p*=0.06, D=0.08).
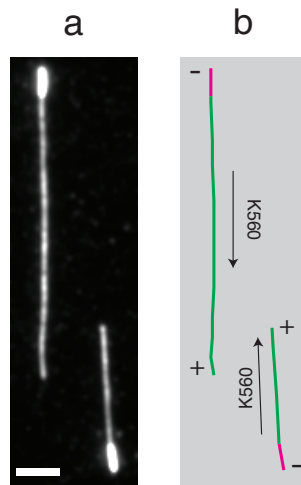
Fig. S10. Polarity-marked MTs. (*A*) Fluorescence image of polarity-marked MTs (scale bar: 3 μm). The bright ends are the "seeds" from which plus-end polymerization was nucleated. (*B*) Schematic diagram showing bright plus ends (magenta) on less densely labeled MTs (green). Kinesin K560, an exclusively plus-end-directed motor, consistently walked away from the bright ends.
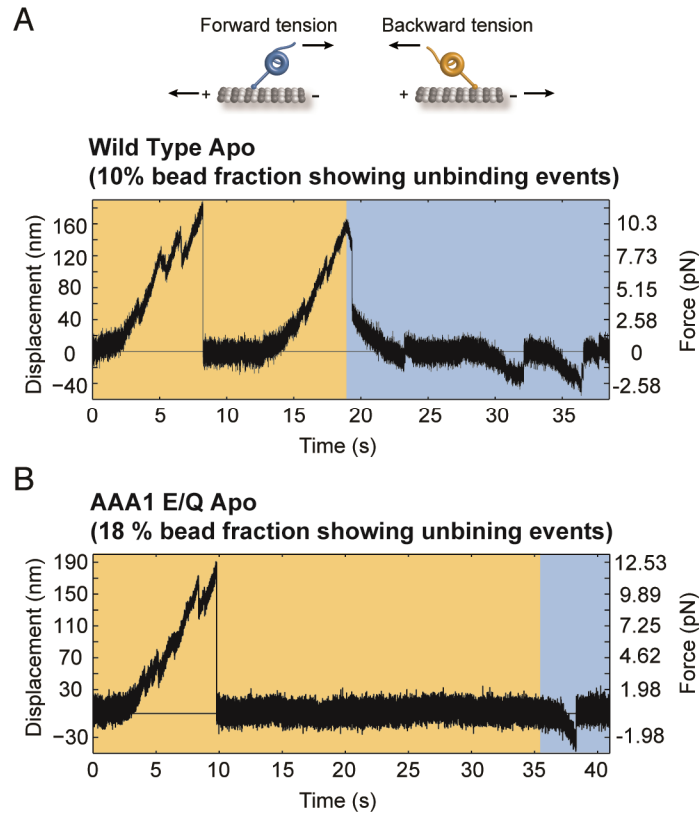
Fig. S11. Unbinding-force experiments (force/position vs. time) in the absence of nucleotide (ATP and ADP depleted with apyrase) for the wild-type motor domain (*A*) and the ATP-hydrolysis AAA1 E/Q mutant (*B*). The illustration in *A* represents the configuration for backward vs. forward tension. Orange (blue) shaded areas show periods of applied rearward (forward) tension. The loading rate was 5.6 pN/s ($k \approx 0.07$ pN/nm, $v_{stage} \approx 80$ nm/s). Experiments were performed at concentrations of dynein to produce MT binding by 10% (*A*) and 18% (*B*) of beads in the final assay, implying binding by single motors (*38*).
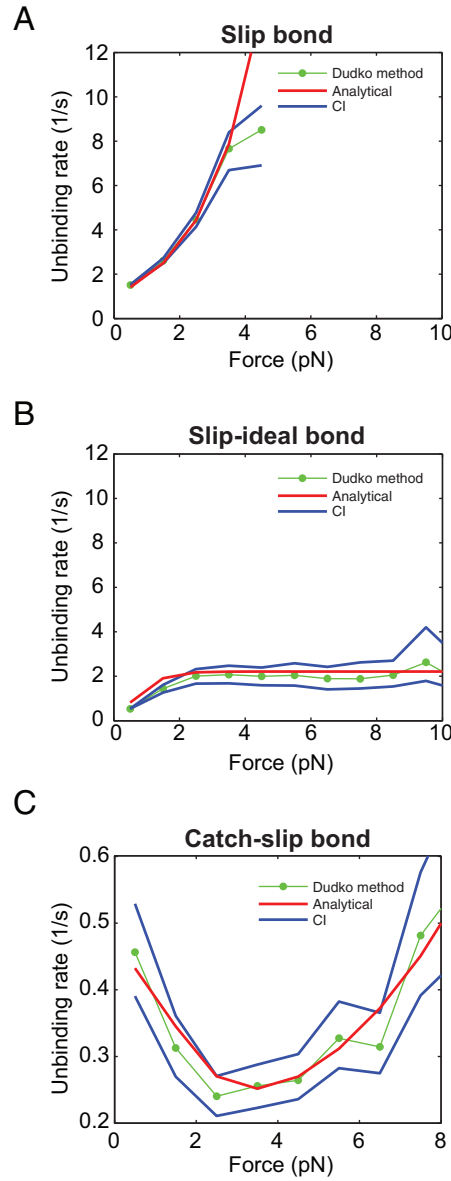
Fig. S12. Computational validation of the Dudko-method for three different bond behaviors. In all graphs, the green points are the calculated unbinding rates from the Dudko-method applied to data from rupture-force simulations of stochastic bond models depicted in this figure. The red lines are analytical solutions of these models. The areas between the blue lines represent 95% confidence intervals (CIs) estimated by bootstrapping with 4000 samples. The models and the simulation procedures are described in detail in the Supplemental Information. (*A*) A typical slip-bond behavior showing an exponentially increasing unbinding rate as a function of force. Originally, the Dudko-method was developed to study such a bond (*60*). For the simulation of the rupture-force histograms we used a loading rate of 5.6 pN/nm and 575 unbinding events, as was the case for the Apo state forward unbinding-force experiments of the WT motor (Fig. 1E). (*B*) The unbinding rate of a slip-ideal bond first increases with increasing force and then saturates so that the unbinding rate becomes load insensitive. This behavior describes the backward unbinding-force experiments of the WT motor in the Apo state as shown in Figs. 1E and 1G. In the simulations we used a loading rate of 5.6 pN/nm and 512 unbinding events as for the corresponding experiment. (*C*) The unbinding rate of a catch-slip bond first decreases and then increases as a function of force. For the simulation we used a loading rate of 1 pN/nm and 600 unbinding events for the analysis.